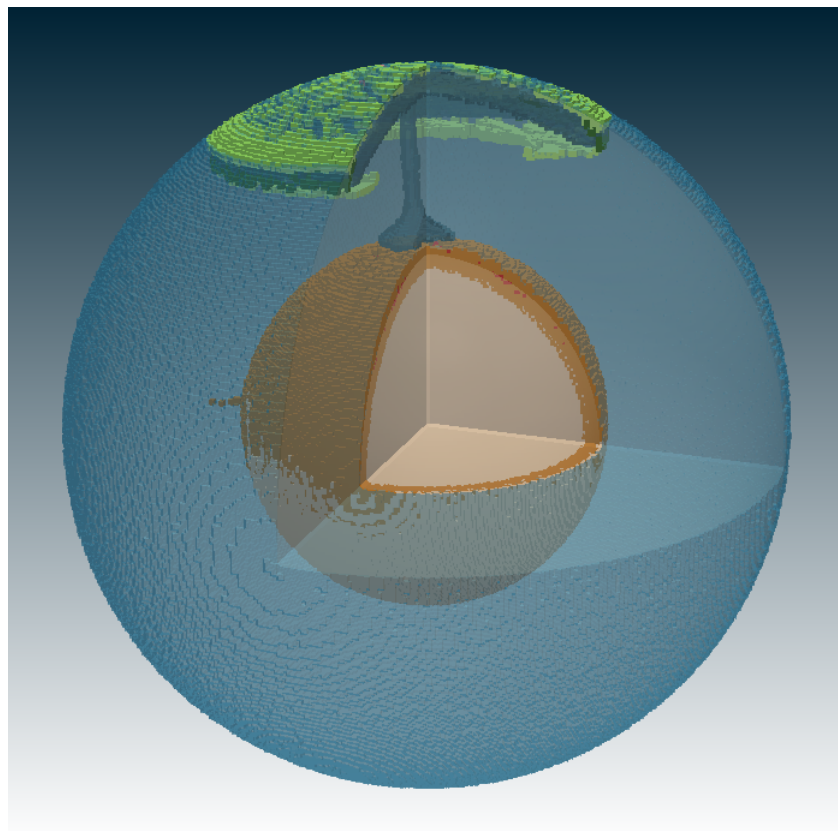# Adaptive Multigrid.
How to couple Adaptive Mesh Refinement with the Multigrid method.
and
Self-consistent modelling of planetary differentiation and onset of mantle convection on Mars.
A comparative study in 2D and 3D

by Ria Fischer

Master Thesis

Department of Earth Sciences
Geophysical Institute
ETH Zurich

Ria Fischer
FS 2012

Adaptive Multigrid.
How to couple Adaptive Mesh Refinement with the Multigrid method.
and
Self-consistent modelling of planetary differentiation and onset of mantle convection on Mars.
A comparative study in 2D and 3D

Zurich
August 2012

Supervisors

Prof. Dr. Taras Gerya
Prof. Dr. James Connolly
Dr. Gregor J. Golabek

ETH
Eidgenössische Technische Hochschule Zürich
Swiss Federal Institute of Technology Zurich

Contents

Abstract

In a first part of this thesis an Adaptive Multigrid solver for conservative finite differences is presented. Adaptive Multigrid makes use of two key-techniques: Adaptive Mesh Refinement, where high resolution is used only where it is needed and Multigrid, an iterative solver, using grids of different resolution in parallel. The presented solver is tested in three different benchmark tests for convergence under high viscosity contrast and found to converge well.

The exact mechanism of core-mantle differentiation and the formation of the crustal dichotomy and the Tharsis rise on Mars, are still unresolved problems. In the second part of this thesis I, therefore, investigate a hypothesis which numerically combines both exogenic and endogenic processes, where a giant impact event and subsequent vigorous mantle convection are building the southern highland crust. In this thesis I focus on the effect, various initial factors have on core and crustal formation. Key factors of interest are the impactor core temperature, the initial planetary iron and silicate temperature, as well as the initial setup and the impactor size. At the impact site a hemispherical magma ocean can be observed which spreads over the planets surface and finally builds one large patch of thicker crust. In the special case of very hot iron diapirs or hot protocore, an additional magma ocean at the depth of the core-mantle boundary develops. In the case of a very hot impactor, the impactor core will form a hot liquid outer core and enable dynamo generation.

Part I.

Adaptive Multigrid.

How to couple Adaptive Mesh Refinement with the Multigrid method.

1. Introduction

In numerical modelling, the usual way to go, is to produce a set of linear equations, which can be solved for all the unknowns at each node in the predefined grid. Normally the grid spacing is chosen as fine as possible for maximum resolution in the output model, the confining quantity being mainly computational power.

The computational power required can be reduced by introducing the technique of Adaptive Mesh Refinement (AMR). With AMR the grid spacing is generally rather coarse but is refined in areas where it is required.

Still the use of direct solvers to solve for the system of linear equations places strong limitations on the maximum number of nodes (Gerya, 2010). Especially in 3D where the amount of equations is much larger, one therefore has to fall back on iterative methods (Gerya, 2010).

In this first part of this thesis I test the possibility of combining AMR with an iterative solver like Multigrid in 2D.

Part I is structured as follows: section 2 gives an overview over both methods AMR and Multigrid and describes how they could be combined, section 3 discusses some benchmark tests with the new Adaptive Multigrid method, while section 4 presents the findings and section 5 gives a short summary and outlook.

2. Methods

2.1. The finite difference method on a staggered grid

There are two basic principles of solving a partial differential equation (PDE), analytical and numerical. The finite-difference-method (FDM) is one of the most simple and basic approaches for programming numerical models. Finite differences are linear mathematical operators. Derivatives can be represented by finite differences within a certain degree of accuracy in the following way,

$$\frac{\partial \Phi}{\partial x} = \frac{\Delta \Phi}{\Delta x} = \frac{\Phi_2 - \Phi_1}{x_2 - x_1}, \tag{2.1}$$

where $\Delta \Phi = \Phi_2 - \Phi_1$ represents the difference in the field variable of interest and $\Delta x = x_2 - x_1$ represents the difference in x-direction. With smaller Δx the accuracy of the computed derivative is increasing.

An infinite amount of points in a continuous medium is now replaced with a finite amount of grid points. All physical properties that are needed (like for example density ρ, viscosity η, velocity v_x, v_y, v_z or pressure P) are defined at these grid points. In the case of thermo-mechanical numerical problems with variable viscosity and when the continuity, Stokes or temperature equations are formulated in 2D or 3D, the choice of a fully staggered grid (Fig 1) is the most convenient one, because the finite-difference formulation becomes more natural and simple (Gerya, 2010). Using a fully staggered grid instead of a non-staggered, even the accuracy of the numerical solution is up to four times higher (Gerya, 2010).

The desired PDE (including boundary condition equations) is now applied to the grid points. At each grid point, the PDE is substituted by a linear equation by making use of the finite difference operator (eqs. (2.1)). For example the Stokes equation (see part II chp. 2 for a more detailed discussion) in x-direction,

$$\frac{\partial \sigma'_{xx}}{\partial x} + \frac{\partial \sigma'_{xy}}{\partial y} - \frac{\partial P}{\partial x} = -\rho(x,y)g_x \tag{2.2}$$

reads like this in finite difference formulation (compare Fig. 1),

$$\frac{\sigma'_{xxB} - \sigma'_{xxA}}{\Delta x} + \frac{\sigma_{xy2} - \sigma_{xy1}}{\Delta y} - \frac{P_B - P_A}{\Delta x} = -\frac{\rho_1 + \rho_2}{2}g_x \tag{2.3a}$$

$$\sigma_{xy1} = \eta_1 \left(\frac{v_{x3} - v_{x2}}{\Delta y} + \frac{v_{y3} - v_{y1}}{\Delta x} \right) \tag{2.3b}$$

●v_x, q_z ○v_z, q_x ■$\varepsilon_{xz}, \sigma_{xz}, T, \eta, \rho, k, Cp, \alpha$ □$P, \varepsilon_{xx}, \varepsilon_{zz}, \sigma_{xx}, \sigma_{zz}$
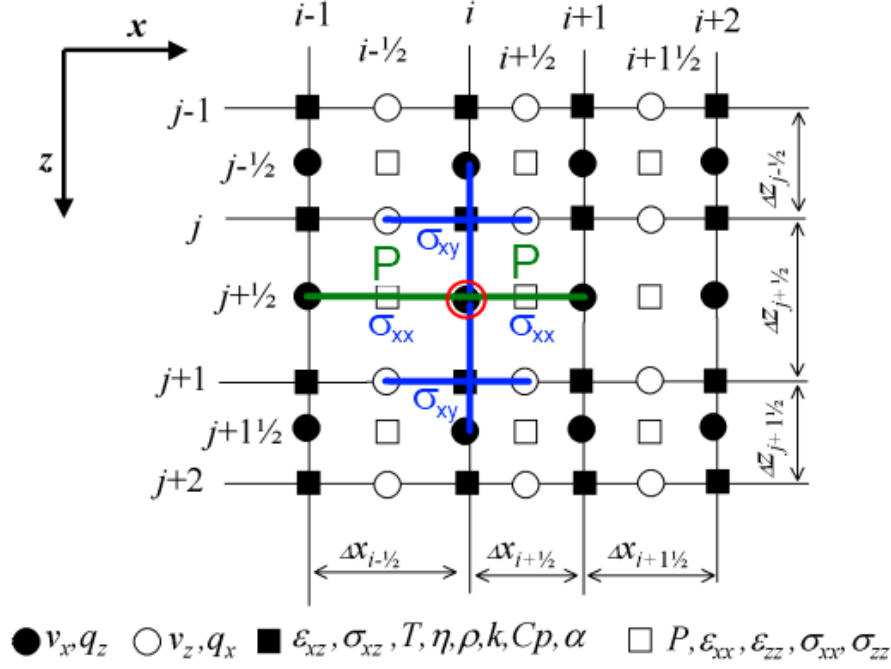
Figure 1: Example of a fully staggered grid in 2D. The expression for the x-Stokes equation (2.3) is marked and the red circle marks the node which is being evaluated.

$$\sigma_{xy2} = \eta_2 \left(\frac{v_{x4} - v_{x3}}{\Delta y} + \frac{v_{y4} - v_{y2}}{\Delta x} \right) \tag{2.3c}$$

$$\sigma'_{xxA} = 2\eta_A \frac{v_{x3} - v_{x1}}{\Delta x} \tag{2.3d}$$

$$\sigma'_{xxB} = 2\eta_B \frac{v_{x5} - v_{x3}}{\Delta x} \tag{2.3e}$$

This way a system of linear equations is built by formulating the Stokes equation in each direction and the continuity equation for each node, all in all five equations for each cell. This system of linear equations has the following general form, where S_k denotes the unknowns, $L_{k,l}$ the coefficients and R_k the right-hand side,

$$\begin{aligned}
L_{1,1}S_1 + L_{1,2}S_2 + L_{1,3}S_3 + \cdots + L_{1,n-1}S_{n-1} + L_{1,n}S_n &= R_1 \\
L_{2,1}S_1 + L_{2,2}S_2 + L_{2,3}S_3 + \cdots + L_{2,n-1}S_{n-1} + L_{2,n}S_n &= R_2 \\
\cdots & \\
L_{n-1,1}S_1 + L_{n-1,2}S_2 + L_{n-1,3}S_3 + \cdots + L_{n-1,n-1}S_{n-1} + L_{n-1,n}S_n &= R_{n-1} \\
L_{n,1}S_1 + L_{n,2}S_2 + L_{n,3}S_3 + \cdots + L_{n,n-1}S_{n-1} + L_{n,n}S_n &= R_n
\end{aligned} \tag{2.4a}$$

$$\begin{pmatrix} L_{1,1} & L_{1,2} & L_{1,3} & \cdots & L_{1,n-1} & L_{1,n} \\ L_{2,1} & L_{2,2} & L_{2,3} & \cdots & L_{2,n-1} & L_{2,n} \\ & & & \cdots & & \\ L_{n-1,1} & L_{n-1,2} & L_{n-1,3} & \cdots & L_{n-1,n-1} & L_{n-1,n} \\ L_{n,1} & L_{n,2} & L_{n,3} & \cdots & L_{n,n-1} & L_{n,n} \end{pmatrix} \begin{pmatrix} S_1 \\ S_2 \\ S_3 \\ \vdots \\ S_{n-1} \\ S_n \end{pmatrix} = \begin{pmatrix} R_1 \\ R_2 \\ R_3 \\ \vdots \\ R_{n-1} \\ R_n \end{pmatrix} \tag{2.4b}$$

$$LS = R \tag{2.4c}$$

To solve the system of linear equations, one can choose between two different methods: direct or iterative method.

One of the most common direct solvers is the *Gaussian elimination*. The main advantages of direct solvers are, that no iterations are needed and the solutions are accurate to computer accuracy. The disadvantages are heavy memory usage, proportional to the square of the number of unknowns, and large number of operations needed, also to the cube of the number of unknowns (Gerya, 2010).

Still if high resolution is required or the model is in 3D, the large number of equations might be too much to be handled by a direct solver. The alternative is using iterative solvers, which have a few advantages because they only alter one equation at a time and therefore, only two to three equations, depending on the solver, have to be loaded into memory. The amount of memory consumed is typically proportional to the number of unknowns. Also a smaller amount of operations is needed, proportional to the number of unknowns per solution cycle. Disadvantages of iterative methods are lower accuracy of the solution and problems of convergence towards an accurate solution (Gerya, 2010).

There are several different iterative methods. Two of the most common are the *Jacobi iteration* and the *Gauss-Seidel iteration* (GS). In the Jacobi iteration the unknowns are updated simultaneously after finishing one iteration, whereas in the Gauss-Seidel iteration the value for each unknown is updated separately during the course of one iteration as soon as it is obtained.

For iterative methods to begin with, an initial guess for the solution vector S is needed. Often $S_k^{initial} = 0$ is chosen. Then the *residuum*, the difference between actual right-hand side and right-hand side calculated from the current solution, is computed as follows,

$$\Delta R_1 = R_1 - L_{1,1}S_1^{current} - L_{1,2}S_2^{current} - L_{1,3}S_3^{current} - \cdots$$
$$-L_{1,n-1}S_{n-1}^{current} - L_{1,n}S_n^{current}$$
$$\Delta R_2 = R_2 - L_{2,1}S_1^{current} - L_{2,2}S_2^{current} - L_{2,3}S_3^{current} - \cdots$$
$$-L_{2,n-1}S_{n-1}^{current} - L_{2,n}S_n^{current}$$
$$\cdots \qquad (2.5)$$
$$\Delta R_{n-1} = R_{n-1} - L_{n-1,1}S_1^{current} - L_{n-1,2}S_2^{current} - L_{n-1,3}S_3^{current} - \cdots$$
$$-L_{n-1,n-1}S_{n-1}^{current} - L_{n-1,n}S_n^{current}$$
$$\Delta R_n = R_n - L_{n,1}S_1^{current} - L_{n,2}S_2^{current} - L_{n,3}S_3^{current} - \cdots$$
$$-L_{n,n-1}S_{n-1}^{current} - L_{n,n}S_n^{current}$$

The residuals $\Delta R_1, \Delta R_2, \cdots, \Delta R_n$ can now be used to obtain a new and more accurate solution $S_1^{new}, S_2^{new}, \cdots, S_n^{new}$ of the unknowns,

$$S_1^{new} = S_1^{current} + \theta_1 \frac{\Delta R_1}{L_{1,1}}$$
$$S_2^{new} = S_2^{current} + \theta_2 \frac{\Delta R_2}{L_{2,2}}$$
$$\cdots \qquad (2.6)$$
$$S_{n-1}^{new} = S_{n-1}^{current} + \theta_{n-1} \frac{\Delta R_{n-1}}{L_{n-1,n-1}}$$
$$S_n^{new} = S_n^{current} + \theta_n \frac{\Delta R_n}{L_{n,n}}$$

The *relaxation parameters* $\theta_1, \theta_2, \cdots, \theta_n$ define how strongly the new solutions are influenced by the residuals and are usually in the range between 0.5 and 1.5.

The iterative step from eq. (2.6) now has to be repeated until the error reaches an acceptable level. To speed up this process, initial guess $S_k^{initial}$ and relaxation parameters θ_k should be chosen appropriately.

2.2. Adaptive Mesh Refinement

Often when high resolution is desired, it is actually only needed in a very small, very specific area of the model. It is therefore no loss, if the rest of the model has a much lower resolution. Fig. 2 for example, has high resolution at the fault zones. In this case the main interest are the fault zones and outside the fault zones much lower resolution is acceptable as well.

The AMR technique makes use of this and starts out with a regular basic grid with very low resolution. Then an upper and lower threshold for cell splitting and merging are defined. As soon as the contrast between two cells in the variable of interest breaches the threshold, these

cells are refined. On the other hand, if the contrast drops below a lower threshold, the cells are merged. After each timestep the grid is adjusted according to these criteria, where cells can be either split up or merged. Common examples for splitting and merging of cells are for example velocity and pressure gradient. In Fig. 2 the criterion for merging and splitting is strain rate.

This finally leads to an irregular grid with low resolution in areas of a low gradient in the variable of interest and high resolution in areas of a steep gradient in the variable of interest. Therefore, without significantly lowering the accuracy, the amount of nodes and finally, the number of linear equations and consequentially, computational power needed is much lower.
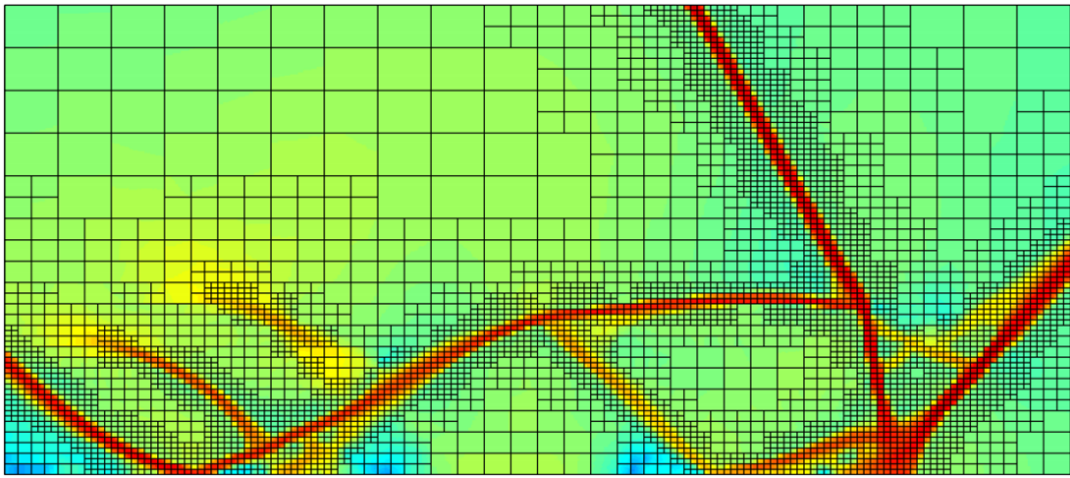

Figure 2: Example of an AMR grid with strain rate as splitting and merging criterion (Mishin et al., 2010).

A few requirements have to be fulfilled, to make the use of AMR easier. Only rectangular blocks in structured grids are allowed. A refinement step splits the cell into four equal sized smaller squares. A merging step joins four neighbouring cells into one larger cell. The difference in resolution at resolution boundaries can never be larger than one. See Fig. 8. No two of the differently coloured resolution boundaries can fall together.

Special care has to be given to the finite difference formulation at resolution boundaries. If many values are interpolated outside the resolution boundary like in Fig. 3a the resulting finite difference formulation as it was suggested by Albers (2000) cannot conserve stresses. On the other hand, stresses are conserved if the grid is chosen as shown in Fig. 3b and less values are interpolated (Gerya et al., prep).

At resolution boundaries the most fitting stencils have to be found, for each possible configuration of small and large cells, separately (Gerya et al., prep). Gerya et al. (prep) employed two different principles to interpolate for velocity on a finer level (marked with red triangles

and red squares in Fig. 3b): (i) conservation of volume flux across resolution boundaries and (ii) stress-based interpolation of velocity gradients. Fig. 4a gives an example for a stencil of the x-Stokes equation on the fine grid side of the resolution boundary and Fig. 4b gives an example for a stencil of the y-Stokes equation on the coarse grid side of the resolution boundary.
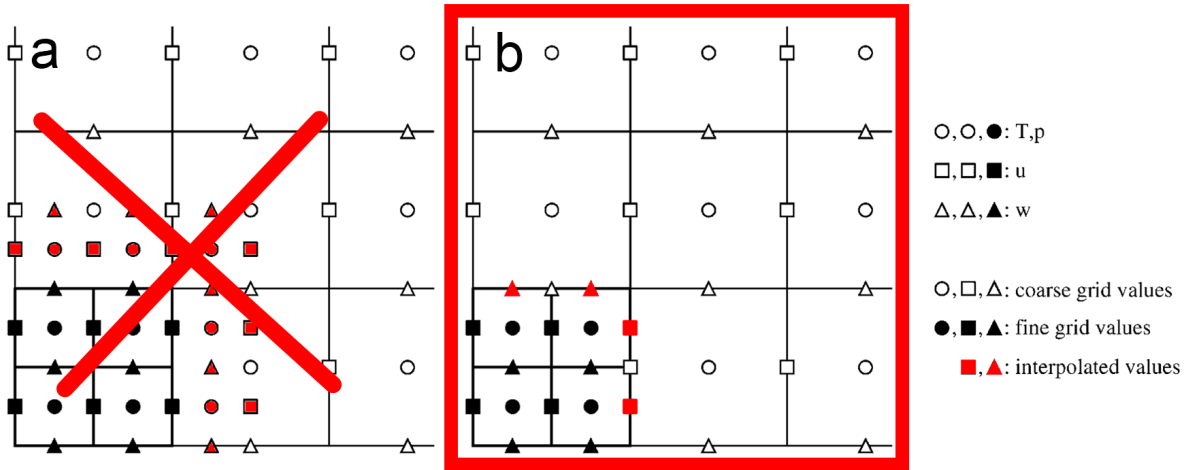
Figure 3: (a) Interpolated values should not be chosen this way at resolution boundaries, because this will lead to a non-conservative finite-difference formulation (Albers, 2000). (b) Instead, if the interpolated values at resolution boundaries are chosen this way, the finite-difference formulation will conserve stresses (Gerya et al., prep).
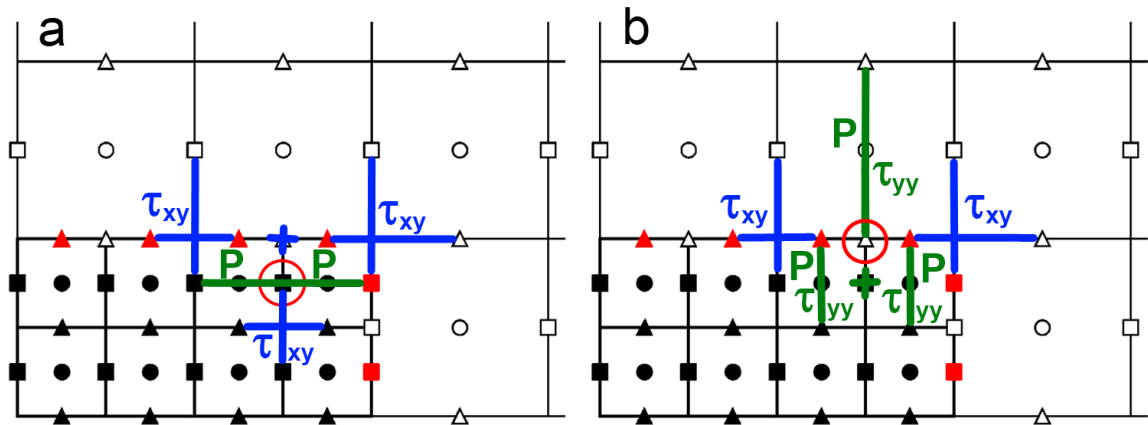
Figure 4: (a) X-Stokes stencil on a fine grid and (b) y-Stokes stencil on a coarse grid.(Gerya et al., prep)

To make the above proposed finite-difference formulation programmatically possible, the following precautions have been taken. (1) Each basic node (green plus signs in Fig. 5) is given a unique index. (2) Each cell (blue crosses in Fig. 5) is given a unique index as well. To ensure

node to cell connectivity, (3) indexes for all four surrounding cells are listed for every node (blue arrows in Fig. 5) and (4) indexes for all four surrounding nodes are listed for every cell (green arrows in Fig. 5). (5) Now five equations are composed for each cell: two from the two v_x nodes, two in the two v_y nodes and one in the pressure node.
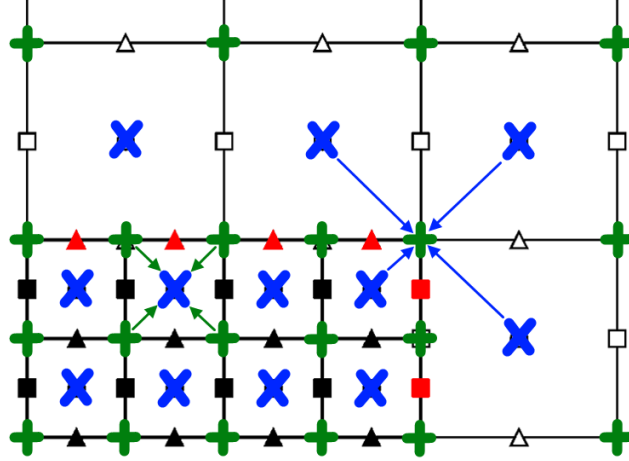

Figure 5: Grid connectivity: (1) Green plus signs show basic nods, (2) blue crosses show cells, (3) blue arrows show cells to node connectivity and (4) green arrows show nodes to cell connectivity.

2.3. Multigrid

The major drawback of iterative methods is, that with increasing resolution, the number of iterations needed to reach a certain level of convergence, increases as well. Multigrid offers a solution, as the number of iterations with Multigrid, is independent of the number of nodes (Gerya, 2010). This can be achieved by simultaneously solving the same equations in parallel on different grids with different resolutions (Gerya, 2010). Therefore, also the name: MULTI-grid.

Multigrid is based on the idea that any linear equation or system of linear equations (eq. (2.4)) can be represented in additive form, where the unknowns are the sum of the current, known approximations $S_1^{current}, S_2^{current}, \cdots, S_n^{current}$ of $S_1, S_2, \cdots, S_n$ and unknown correc-tions $\Delta S_1, \Delta S_2, \cdots, \Delta S_n$ are needed to fulfil eq. (2.4a).

$$
\begin{aligned}
S_1 &= S_1^{current} + \Delta S_1 \\
S_2 &= S_2^{current} + \Delta S_2 \\
&\cdots \\
S_n &= S_n^{current} + \Delta S_n
\end{aligned}
\tag{2.7}
$$

The corrections $\Delta S_1, \Delta S_2, \cdots, \Delta S_n$ are fulfilling the following equation:

$$
\begin{aligned}
L_{1,1}\Delta S_1 + L_{1,2}\Delta S_2 + \cdots + L_{1,n}\Delta S_n &= \Delta R_1 \\
L_{2,1}\Delta S_1 + L_{2,2}\Delta S_2 + \cdots + L_{2,n}\Delta S_n &= \Delta R_2 \\
&\cdots \\
L_{n,1}\Delta S_1 + L_{n,2}\Delta S_2 + \cdots + L_{n,n}\Delta S_n &= \Delta R_n
\end{aligned}
\tag{2.8}
$$

where the right-hand side is given by the current residuals from the original system of linear equations.

$$
\begin{aligned}
\Delta R_1 &= R_1 - \left(L_{1,1}S_1^{current} + L_{1,2}S_2^{current} + \cdots + L_{1,n}S_n^{current}\right) \\
\Delta R_2 &= R_2 - \left(L_{2,1}S_1^{current} + L_{2,2}S_2^{current} + \cdots + L_{2,n}S_n^{current}\right) \\
&\cdots \\
\Delta R_n &= R_n - \left(L_{n,1}S_1^{current} + L_{n,2}S_2^{current} + \cdots + L_{n,n}S_n^{current}\right)
\end{aligned}
\tag{2.9}
$$

But when some approximations to the corrections ΔS_k are known, the corrections can also be represented in additive form with known approximations to the corrections $\Delta S_1^{current}, \Delta S_2^{current}, \cdots, \Delta S_n^{current}$ and unknown corrections to the corrections $\Delta\Delta S_1, \Delta\Delta S_2, \cdots, \Delta\Delta S_n$.

$$
\begin{aligned}
\Delta S_1 &= \Delta S_1^{current} + \Delta\Delta S_1 \\
\Delta S_2 &= \Delta S_2^{current} + \Delta\Delta S_2 \\
&\cdots \\
\Delta S_n &= \Delta S_n^{current} + \Delta\Delta S_n
\end{aligned}
\tag{2.10}
$$

The corrections of the corrections $\Delta\Delta S_1, \Delta\Delta S_2, \cdots, \Delta\Delta S_n$ are again fulfilling the same system of linear equations with *the same coefficients $L_{k,l}$*:

$$
\begin{aligned}
L_{1,1}\Delta\Delta S_1 + L_{1,2}\Delta\Delta S_2 + \cdots + L_{1,n}\Delta\Delta S_n &= \Delta\Delta R_1 \\
L_{2,1}\Delta\Delta S_1 + L_{2,2}\Delta\Delta S_2 + \cdots + L_{2,n}\Delta\Delta S_n &= \Delta\Delta R_2 \\
&\cdots \\
L_{n,1}\Delta\Delta S_1 + L_{n,2}\Delta\Delta S_2 + \cdots + L_{n,n}\Delta\Delta S_n &= \Delta\Delta R_n
\end{aligned}
\tag{2.11}
$$

but with a slightly different right-hand side $\Delta\Delta R_1, \Delta\Delta R_2, \cdots, \Delta\Delta R_n$, which is now the current residuum of eq. (2.8):

$$\Delta\Delta R_1 = \Delta R_1 - \left(L_{1,1}\Delta S_1^{current} + L_{1,2}\Delta S_2^{current} + \cdots + L_{1,n}\Delta S_n^{current}\right)$$
$$\Delta\Delta R_2 = \Delta R_2 - \left(L_{2,1}\Delta S_1^{current} + L_{2,2}\Delta S_2^{current} + \cdots + L_{2,n}\Delta S_n^{current}\right)$$
$$\cdots$$
$$\Delta\Delta R_n = \Delta R_n - \left(L_{n,1}\Delta S_1^{current} + L_{n,2}\Delta S_2^{current} + \cdots + L_{n,n}\Delta S_n^{current}\right)$$

(2.12)

Of course also corrections to the corrections of the corrections can be found.

The key to the Multigrid method is now that each of the systems of linear equations (2.4a), (2.8) and (2.11) for the same numerical model is solved on a different numerical grid.

The finest grid (Level 1, see Fig. 6) is the principal grid and the one on which the actual solution is desired. On this grid eq. (2.4a) is solved by Gauss-Seidel iteration. Residuals and transport coefficients are now interpolated to a coarser level (restriction operation), where eq. (2.8) is again solved by Gauss-Seidel iteration. This process is repeated as often as desired. The solution on the coarsest grid is obtained either by a large amount of Gauss-Seidel iterations or by a direct solver. The correction to the solution is now prolonged on to the next finer grid, where it corrects the approximate solution there, which again is prolonged on to the next finer grid and so on. Until the chain of prolonged corrections reaches the solution on the principal grid again and the final solution is obtained.

This cycle of restrictions down to the coarsest level, followed by prolongations up again to the finest level is called the V-cycle (Fig. 7) and is the classical Multigrid iteration cycle. Other possible iteration cycles include the W-cycle, the F-cycle and the sawtooth-cycle (Fig. 7), but are less common.

For a more in-depth discussion of the here discussed Multigrid method see also Gerya (2010).

2.3.1. Computational compressibility: Solving Stokes and Continuity equations

One of the main problems with the Multigrid method is solving the coupled momentum and continuity equations and finding an appropriate smoothing algorithm. The finite difference operation of the continuity equation is formulated at the pressure nodes and leads to a zero entry in the main diagonal for the incompressible continuity equation ($L_{i,i} = 0$ in equation (2.6)).

A solution offers the computational compressibility approach (Gerya, 2010). Computational compressibility factor $\beta_{i,j}^{computational}$ is chosen for pressure updates,

$$\Delta R_{i,j}^{continuity} = R_{i,j}^{continuity} - \nabla \times \vec{v}_{i,j},$$
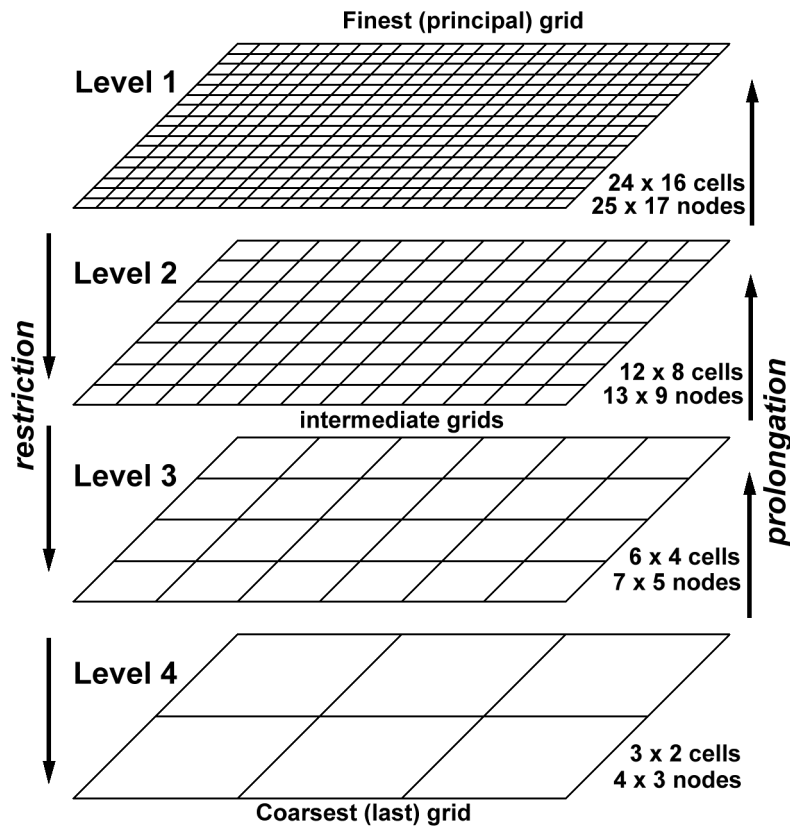
(2.13a)

Figure 6: Multigrid works on different levels with grids of different resolutions. Restriction and prolongation operations are connecting the different levels (Gerya, 2010).
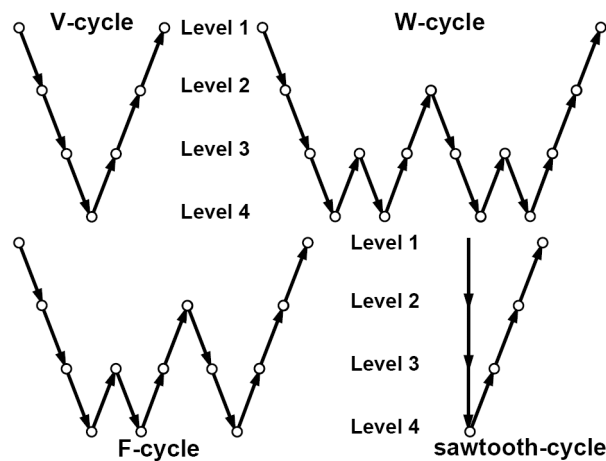

Figure 7: Different Multigrid iteration cycles. Down pointing arrows denote a restriction operation, Up pointing arrows denote a prolongation operation. Most often used is the V-cycle (Gerya, 2010).

$$P_{i,j}^{new} = P_{i,j} + \frac{\Delta R_{i,j}^{continuity}}{\beta_{i,j}^{computational}} \theta_{relaxation}^{continuity}, \qquad (2.13\text{b})$$

The most simple choice for $\beta_{i,j}^{computational}$ is the following,

$$\beta_{i,j}^{computational} = \frac{1}{\eta_{i,j}}, \qquad (2.14)$$

where $\eta_{i,j}$ is the local viscosity.

2.4. Adaptive Multigrid: Combining Adaptive Mesh Refinement and Multigrid

When AMR is used, the linear system of equations is first assembled from the grid, then solved for by any kind of solver. Afterwards the grid is refined and coarsened where necessary. If AMR is supposed to be used with a Multigrid solver, the Multigrid solver has to be adjusted to the irregular grid.

The principal grid for the Adaptive Multigrid is an irregular grid with different levels of resolution (e.g. Fig. 2). On this first level the linear system of equations is assembled as discussed in chapter 2.2 and partially solved by using GS iterations. But instead of coarsening the whole grid, the next V-cycle level uses a grid which is only coarsened in cells of maximum resolution (Fig. 6). This means that the restriction operations have to be executed only for the coarsened cells and not for the whole grid.

This step is now repeated until all cells are at lowest resolution and the grid is uniform. This grid is defined as the coarsest level of the V-cycle. Optionally one could also continue with regular Multigrid restriction steps, coarsening the whole grid.

In the prololongation operation it should be taken care, that the grid on each level is refined in such a way that it does not differ from the grid on the same level during the restriction operation. This is not a problem in regular Multigrid as with coarsening and refining the whole grid, the grid must have the same structure in the end. To solve this problem with Adaptive Multigrid, a possible solution is to save the cell to node and node to cell connections as suggested in Fig. 5 for each level.

Additionally, to make reusing of the solution as an initial guess for the Adaptive Multigrid solver possible, the solution from the old timestep has to be interpolated onto the new grid, as grid structure changes after each timestep, due to AMR.
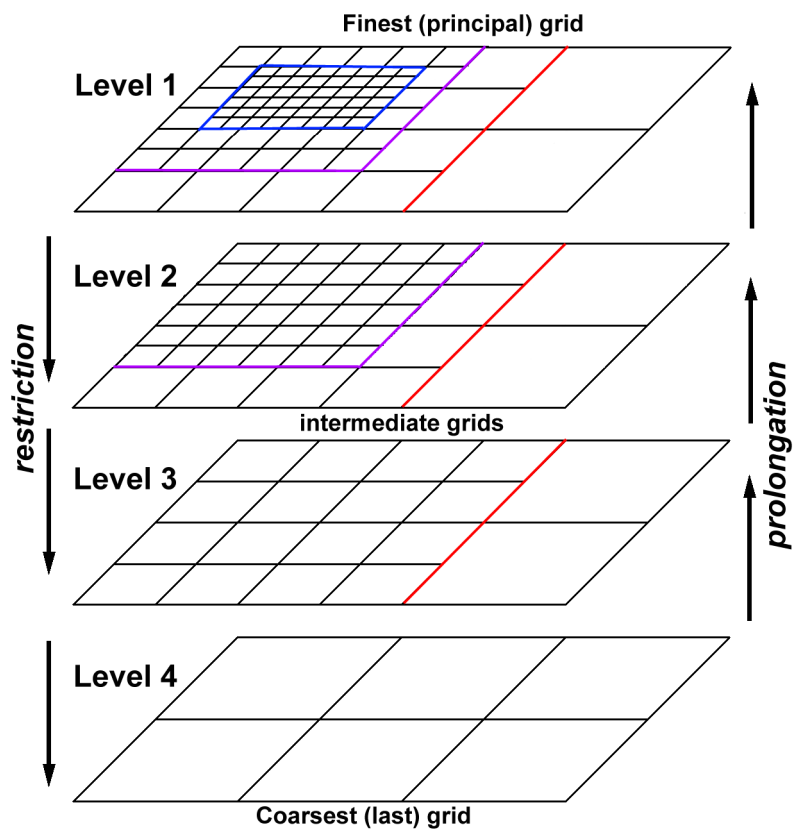
Figure 8: Instead of coarsening the whole grid, in one coarsening step of an Adaptive Multigrid step, the findest level of resolution is removed. Resolution boundaries are marked in different colours.

3. Benchmark testing

This method of combined AMR and Multigrid is specifically developed for applications in geo-dynamics. One of the major challenges in geodynamic modelling are large viscosity contrasts. Therefore, this code is mainly tested for convergence for cases with large viscosity contrast.

For this reason three different benchmark tests have been performed. There is an analytical solution for all of them, which has the advantage of an easy error assessment.

Each test is started with a regular grid of 4×4 points and run for 5 refinement steps. After each step one refinement can be made, which leads to an effective resolution of 49×49 points. One test is started with a regular grid of 3×3, leading to an effective resolution of 33×33.

Parameter	Symbol	Value
Initial number of nodes in horizontal direction	Nx	3
Initial number of nodes in vertical direction	Ny	3
Relaxation parameter for Continuity equation	*theta_cont*	0.8
Relaxation parameter for Stokes equation	*theta_stokes*	0.6
# of iterations at finest level	*niter_min*	10
# of iterations at level before coarsest	*niter_max*	100
# of iterations at coarsest level	*niter_C*	direct
Maximum V-cycle depth	*maxdepth*	5
Number of refinements made	*resmax*	4
Number of timesteps	*stepnumber*	5

Table 1: List of parameters for Adaptive Multigrid

Each V-cycle is only allowed to reach a maximum depth of 5 or until the coarsened grid becomes regular. The solution on the uppermost, finest level is obtained via 10 GS iterations. For each coarser level the amount of GS iterations is linearly increased, up to 100 GS iterations for the second- to-last level. The solution at the coarsest level is obtained by a direct solver.

Benchmark test *SolKz* by Revenaugh and Parsons (1987) (see Fig. 9) has a smooth viscosity field, test *SolCx* by Duretz et al. (2011) (see Fig. 10) has one sharp vertical contrast of $10^6 \, Pa \, s$ in the viscosity field and the *Inclusion* test by Schmid and Podladchikov (2003) has a small inclusion in the viscosity field with a viscosity contrast of $10^3 \, Pa \, s$.
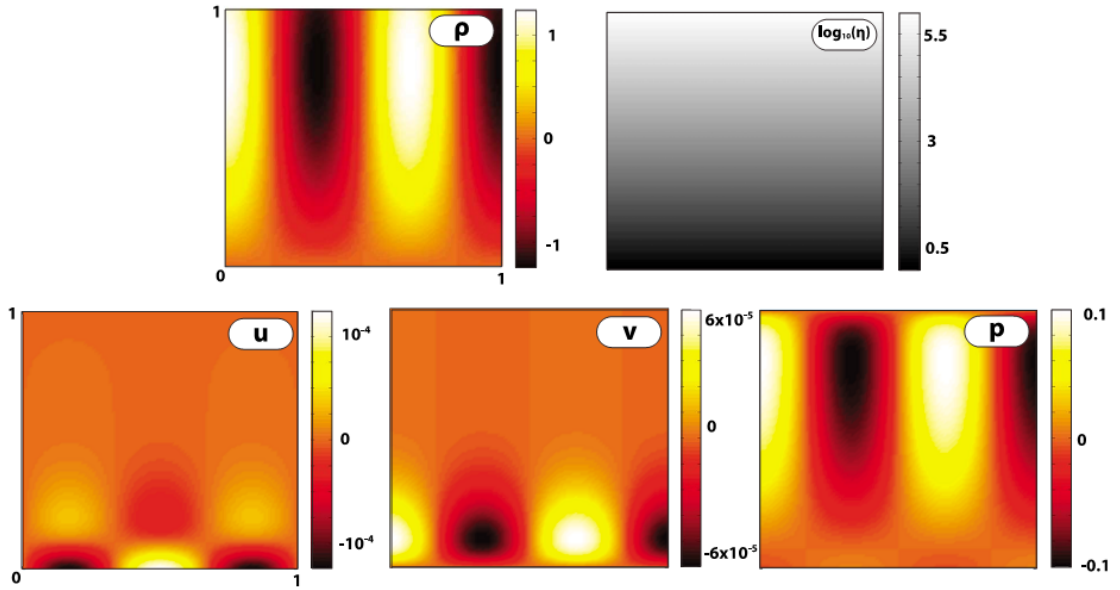
Figure 9: Density (ρ), viscosity (η), and flow pattern (u, v, p) for the analytic solution SolKz (Revenaugh and Parsons, 1987).
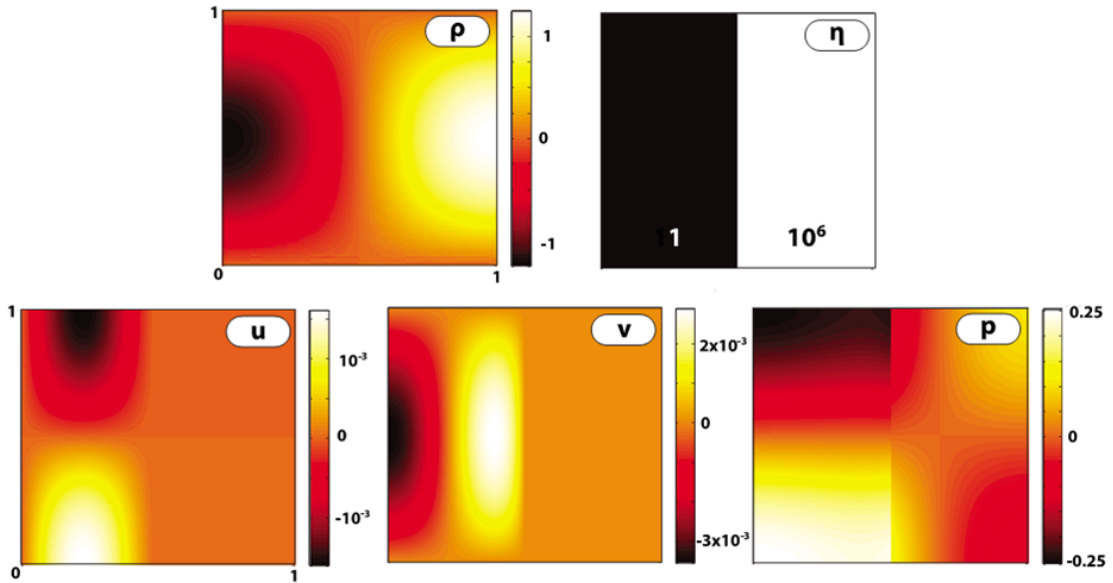
Figure 10: Material properties and the analytic solution for SolCx. The ρ and η are the density and viscosity distributions, u, v are the analytic x, y components of velocity, respectively, and p is the analytic pressure field. The vertical component of gravity acceleration is 1 (Duretz et al., 2011).

Figure 11: Viscosity structure (η) and analytic solution for velocity (u, v) and pressure (p), for the pure shear inclusion test. For this setup, the flow is driven by a strain rate boundary condition ($\dot{\epsilon} = 1$), and the buoyancy forcing term is 0 (e.g., $\rho = 0$ or $g_y = 0$).

4. Results

Figure 12: For each of the three benchmark tests the RMS residuum is shown as a function of V-cycle iterations for the last refinement step. The red line marks a typical machine epsilon.

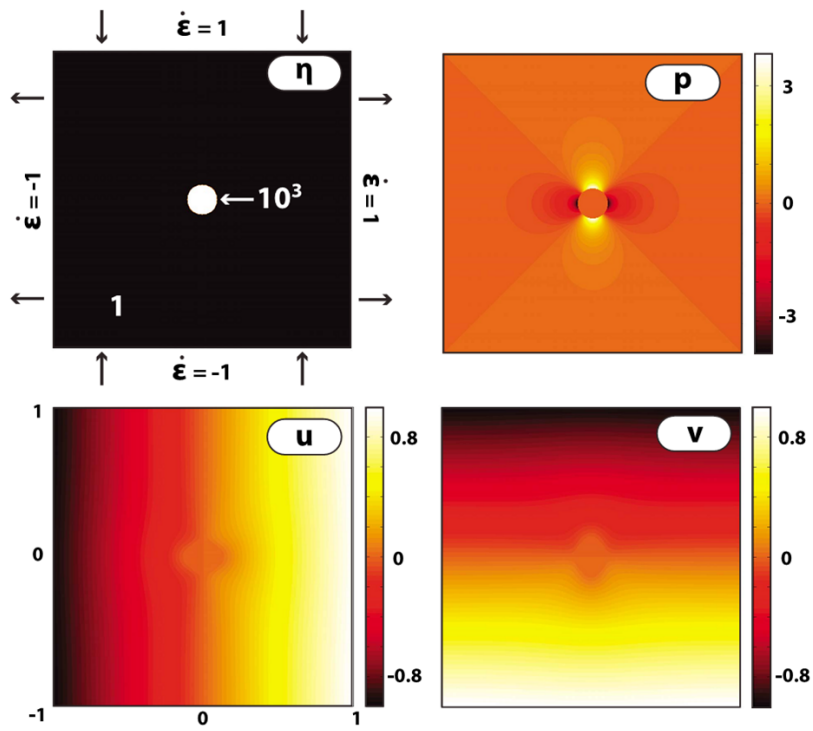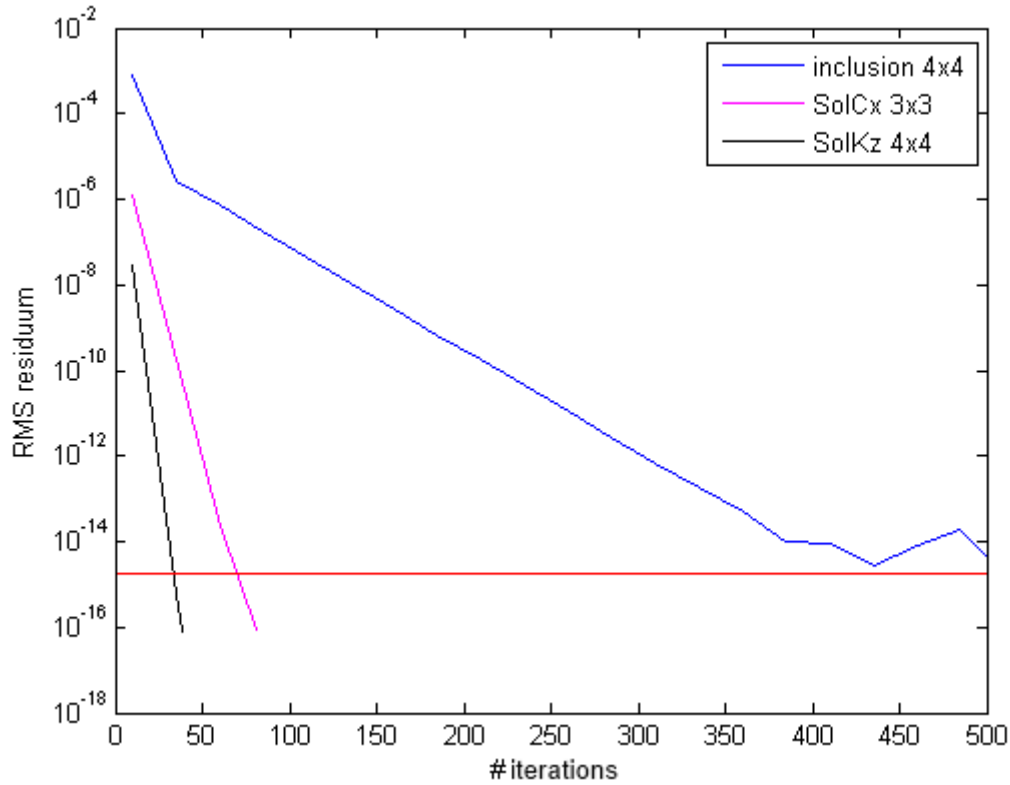For two of the benchmark test, *inclusion* and *SolKz*, a starting resolution of 4×4 nodes has been chosen, resulting in a effective resolution of 49×49 nodes after five refinements. For benchmark test *SolCx* a resolution of 3×3 nodes has been chosen, resulting in an effective resolution of 33×33 nodes after five refinements.

For each of the three benchmark tests, the proposed Adaptive Multigrid solver is tested against the solution of a direct solver. Benchmark test *SolKz* with no sharp viscosity contrast converges fastest, within ~ 50 V-cycles, to a RMS residuum of less than $1.8 \cdot 10^{-15}$, the machine epsilon of the maximum residuum. Benchmark test *SolCx* has a sharp vertical viscosity contrast and reaches machine epsilon after ~ 70 V-cycle iterations.

The inclusion test though seems somewhat harder, due to its small circular 'inclusion' and sharp viscosity contrast at inclusion boundary. More than 350 V-cycle iterations are needed to approach machine epsilon.

5. Conclusion and Outlook

From the benchmark tests it can be concluded that the Adaptive Multigrid method is capable of finding a solution within an error of machine precission within a few $10 - 100$ V-cycle iterations. A next step would be a more thorough testing, also taking into account speed of convergence and finally also implementing this new method into a geodynamic modelling code like for example I2ELVIS (Gerya and Yuen, 2003, 2007).

Adaptive Multigrid is especially well suited for geodynamic problems in need of high resolution and it supports also sharp and strong viscosity boundaries as they are often observed in geodynamic modelling. Adaption of Adaptive Multigrid to 3D still poses some problems, but might help further explore resolution space.

Part II.

Self-consistent modelling of planetary differentiation and onset of mantle convection on Mars.
A comparative study in 2D and 3D

1. Introduction

The main feature on Mars surface is its crustal dichotomy, separating the northern and southern hemisphere. Smooth lowland plains mostly dominate the northern hemisphere, whereas the southern hemisphere is built from heavily cratered highlands. Apart from the topological difference, the dichotomy also appears in tectonics, crater density, gravitational and magnetic field and crustal structure (Watters et al., 2007). The cratering, which cannot only be found on the southern hemisphere but also below the sediments of the northern plains, suggests that both hemispheres formed in the Early Noachian $(4.1 - 3.93\,Ga)$ (Frey, 2006). Therefore, the dichotomy might have well set the course for the geological evolution of the whole planet, playing a major role in the formation of the dominant Tharsis volcanic plateau and the huge valley system Valles Marineris.

Many different models have been proposed to explain this dichotomy. These models can be roughly separated into two different classes. Externally driven models usually assume a giant impact event or multiple smaller impacts that removed part of the northern crust. The impacts happen on the northern hemisphere and the northern lowlands correspond to a huge impact basin. In internally driven models the thinner northern crust is explained by mantle convection, subcrustal erosion due to convective upwelling, or crustal delamination (Watters et al., 2007).

In this second part of this thesis the recently suggested hypothesis by Golabek et al. (2011) will be further investigated. Golabek et al. (2011) suggested a hybrid exogenic-endogenic approach that a giant impact event occurred in the Early Noachian on a Mars formed from already predifferentiated planetesimals. The impact heat would allow to melt large parts of the planets interior, building a hemispherical magma ocean and starting the differentiation. In a second stage, a superplume near the impact site would form the thickened crust in the southern hemisphere and lead to the building of the dichotomy.

Current understanding of terrestrial planet formation indicates planetary accretion by collision with impactors, which become larger with time (Rubie et al., 2007). Towards the end of the accretion process, giant impacts between predifferentiated planetesimals are inevitable. By then, core formation probably already has set in (Rubie et al., 2007). Following the hypothesis by Golabek et al. (2011), the crustal dichotomy would have formed during or soon after accretion and core formation by one last giant impact, roughly the size of $0.1 - 1.0$ lunar masses or around $800 - 1700\,km$ (Reese and Solomatov, 2010). This last, large impact has the potential to introduce a large scale asymmetry into the planets thermal structure, that might produce the crustal structures observed today.

Reese and Solomatov (2010) suggested that an impact of this size might produce huge amounts of silicate melt at the surface, the silicate melt spreading in a hemispherical magma ocean. However for specific temperatures chosen for the silicate as well as the iron of the impactor and the target, they also predicted the formation of a deep seated iron pond formed from iron of the impactor core. This thin ring of liquid iron then could give rise to a short lived Martian dynamo (Reese and Solomatov, 2010).

This second part of this thesis is structured as follows: Section 2 gives an overview of the methods, section 3 describes the model setup, in section 4 the results from the 2D experiments are stated, section 5 depicts the results of the 3D experiments, section 6 shows a comparison between 2D and 3D and discusses the findings. Finally section 7 gives a short summary and outlook.

2. Methods

2.1. Basic physical principals

2.1.1. The continuity equation

The continuity equation describes the conservation of mass, while it is displaced in a continuous medium. In its Lagrangian form it reads the following,

$$\frac{D\rho}{Dt} + \rho\nabla \cdot \vec{v} = 0, \tag{2.1}$$

where ρ denotes material density, $\vec{v}$ denotes displacement velocity and $\frac{D}{Dt}$ denotes the Lagrangian time derivative.

2.1.2. The Poisson equation

The Poission equation describes spatial changes in gravitational potential Φ inside a self-gravitating continuum,

$$\nabla^2\Phi = 4\pi G\rho(x, y, z) \tag{2.2}$$

2.1.3. The Navier-Stokes Euqation

The Navier-Stokes equation of motion in its full form reads the following,

$$\frac{\partial\sigma'_{ij}}{\partial x_j} - \frac{\partial P}{\partial x_i} + \rho g_i = \rho\frac{Dv_i}{Dt}, \tag{2.3}$$

where σ_{ij} is the strain-rate and $\vec{g} = (g_x, g_y, g_z)$ is the gravity vector.

In highly viscous flows the right-hand side of (2.3), the inertial forces $\rho\frac{Dv_i}{Dt}$, is much smaller compared to the gravitational force and can therefore, be neglected. This leads to the *Stokes equation for creeping flow*,

$$\frac{\partial\sigma'_{ij}}{\partial x_j} - \frac{\partial P}{\partial x_i} + \rho g_i = 0. \tag{2.4}$$

Under Boussinesq approximation the density is assumed to be constant, except in the buoyancy force term, where temperature and volatile content play an important role (Gerya and Yuen, 2003). Taking into account the Boussinesq approximation, density $\rho(T, P, c)$ in the buoyancy term ρg_i may vary locally as a function of temperature T, pressure P and composition c,

$$\frac{\partial \sigma'_{ij}}{\partial x_j} - \frac{\partial P}{\partial x_i} = -\rho(T, P, c) g_i. \tag{2.5}$$

2.1.4. Heat conservation equation

The heat conservation equation, also called temperature equation, describes the heat balance in a convective medium, taking into account changes due to internal heat generation, advection and conduction. The Lagrangian heat conservation equation reads as follows,

$$\rho C_p \left(\frac{DT}{Dt} \right) = -\nabla \cdot \vec{q} + H_r + H_a + H_s + H_L, \tag{2.6}$$

with $\vec{q} = -k(T, p, c)\nabla T$, where thermal conductivity $k(T, P, c)$ depends on temperature, pressure and rock composition c. H_r, H_a, H_s, H_L denote radioactive, adiabatic, shear and latent heating.

Adiabatic and shear heating have shown to be important in many tectonic situations, which is why they are not taken as constant (Gerya and Yuen, 2007).

$$H_r = f(c, t) \tag{2.7a}$$

$$H_a = T\alpha\vec{v}\nabla P \tag{2.7b}$$

$$H_s = \sigma'_{ij}\dot{\epsilon}'_{ij} \tag{2.7c}$$

$$H_L = const. \tag{2.7d}$$

The resulting set of the above equations, together with equations (2.5) and (2.7), is called the extended Boussinesq approximations.

2.1.5. Rheology

A visco-plastic rheology is employed (Gerya and Yuen, 2007), with the deviatoric strain-rate $\dot{\epsilon}'_{ij}$ being composed of the following components,

$$\dot{\epsilon}'_{ij} = \dot{\epsilon}'_{ij(viscous)} + \dot{\epsilon}'_{ij(plastic,)} \tag{2.8}$$

where

$$\dot{\epsilon}'_{ij(viscous)} = \frac{1}{2\eta}\sigma'_{ij}, \tag{2.9a}$$

$$\dot{\epsilon}'_{ij(plastic)} = \chi\frac{\partial G}{\partial \sigma'_{ij}} = \chi\frac{\sigma'_{ij}}{2\sigma_{II}} \quad \text{for } G = \sigma_{II} = \sigma_{yield}. \tag{2.9b}$$

where η denotes viscosity, σ'_{ij} denotes the deviatoric stress tensor, G is the plastic potential, σ_{yield} is yield strength, σ_{II} is second deviatoric stress invariant and χ is plastic potential.

Generally the strain tensor ϵ_{ij} can be defined as a function of displacement $\vec{u} = (u_x, u_y, u_z)$,

$$\epsilon_{ij} = \frac{1}{2}\left(\frac{\partial u_i}{\partial x_j} + \frac{\partial u_j}{x_i}\right). \tag{2.10}$$

The viscous constitutive relationship relates stress σ_{ij} with strain ϵ_{ij},

$$\sigma'_{ij} = 2\eta\dot{\epsilon}'_{ij}, \tag{2.11}$$

where σ'_{ij} is the deviatoric stress, $\dot{\epsilon}'_{ij}$ is the deviatoric strain-rate, $\dot{\epsilon}_{kk}$ is the bulk strain-rate, and η and η_{bulk} are shear and bulk viscosity.

The viscosity η is defined as follows,

$$\eta = \left(\frac{2}{\sigma_{II}}\right)^{(n-1)}\frac{F^n}{A_D}exp\left(\frac{E + PV}{RT}\right), \tag{2.12}$$

where A_D, E, V and n are experimentally defined flow parameters, R is the gas constant and F is a dimensionless factor depending on the type of experiment (triaxial compression, simple shear).

2.1.6. Impact treatment

The actual impact is not part of the model. The model only starts after the collision of the impactor with the target body. Processes like crater excavation, redistribution of impactor and parent body material around the planet or decompression melting are not considered. A simplified model takes into account the thermal anomaly created by the impactor. A

region called the isobaric core, of uniform temperature increase and shock pressure around the impactor can be found (Senshu et al., 2002).

$$R_{ic} = 3^{\frac{1}{3}} r_{ic} \tag{2.13}$$

where R_{ic} is the radius of the isobaric core and r_{ic} is the radius of the impactor.

The Thermal anomaly in the isobaric core has been approximated by Monteux et al. (2007) in the following way,

$$\Delta T = \frac{4\pi}{9} \frac{\psi}{F} \frac{\rho_P G R_P^2}{c_P} \tag{2.14}$$

where ψ is the efficiency of conversion of kinetic energy to thermal energy and in this thesis assumed to be 0.3.

Outside the isobaric core, for $r > R_{ic}$, the thermal anomaly ΔT is decaying exponentially, according to the following rule (Senshu et al., 2002; Monteux et al., 2007),

$$T(r) = \Delta T \left(\frac{R_{ic}}{r} \right)^{4.4} \tag{2.15}$$

2.1.7. Computation of crust

Formation of crust is only implemented in the 3D code.

Silicate melt within a certain depth is positively buoyant ($d_{depthmelt} = 2 \cdot 10^5$) and rises up to the surface (Golabek et al., 2011). Only markers with a melt fraction between 1% and 20% are considered for crust formation, as this corresponds roughly to the pyroxene fraction in a fertile mantle (Golabek et al., 2011). Silicate melt on markers fulfilling these criteria is assumed to instantaneously percolate upwards through the mantle and to form the crust at the surface.

2.2. I2ELVIS

To model two-dimensional creeping flow under extended Boussinesq approximation, with both thermal and chemical buoyancy, the conservative finite-difference code I2ELVIS (Gerya and Yuen, 2003, 2007) is used, which operates on a staggered grid and uses the marker-in-cell technique. See also part I, chapter 2 for a more detailed discussion. Silicate material is assumed to have temperature-, pressure-, strain-rate and melt fraction-dependant visco-plastic

rheology. Furthermore, impact heating, batch melting of silicates and phase changes have all been taken into account.

2.3. I3ELVIS

The 3D models have been carried out with the 3D numerical I3ELVIS (Gerya and Yuen, 2003, 2007) code which is based on a conservative finite difference method with a marker-in-cell technique and multigrid solver (Gerya and Yuen, 2007). See also part I, chapter 2 for a more detailed discussion. Additionally, the 3D code also features impact heat, batch melting of silicates and phase changes as discussed in Golabek et al. (2011) for the 2D case. The initial thermal-chemical model setup (including initial conditions, boundary condition and fluid/melt transport mechanism) and numerical approach are kept as similar as possible to the 2D models. Furthermore, the 3D code also features computation of the primordial crust from silicate melt.

Parameter	Symbol	Value	Unit
Radius of planetary body	R_{Mars}	3389	km
Radius of impactor core	r_{ic}	$232 - 500$	km
Radius of final core rel. to R_{planet}	r_{core}	0.5	%
Temperature of impactor core	T_{ic}	$1300 - 2300$	K
Temperature of protocore	T_p	$1300 - 2500$	K
Temperature of diapirs	T_d	$1300 - 2300$	K
Mean temperature of final core	$\bar{T}_c$	$-$	K
Mean temperature of silicate mantle	$\bar{T}_m$	$-$	K
Mean temperature of planetary body	$\bar{T}_{tot}$	$-$	K
Mean density of final core	$\bar{\rho}_c$	$-$	$kg\,m^{-3}$
Mean density of silicate mantle	$\bar{\rho}_m$	$-$	$kg\,m^{-3}$
Mean density of planetary body	$\bar{\rho}_{tot}$	$-$	$kg\,m^{-3}$
Volume fraction of iron (3D)	$f_{Fe,vol}$	0.1	%
Mass fraction of iron (3D)	$f_{Fe,mass}$	0.2	%
Gravitational acceleration surface	g	3.73	$m\,s^{-2}$
Gravitational constant	G	6.672	$N\,m^2\,kg^{-2}$
Efficiency of conversion of kinetic to thermal energy	ψ	0.3	$-$

Table 2: List of parameters

3. Model setup

An overview over all tested models and parameters is given in table 3. All models start at 5.0 million years (Ma) after formation of the calcium-aluminium-rich inclusions (CAI).

3.1. 2D models

To test the hypothesis whether core formation with less radiogenic isotopes is still possible, a self-consistent numerical simulation of a giant impact into a Mars-like target body is performed.

As an initial model and starting point for the 2D modelling the best-fit model from Golabek et al. (2011) is chosen, where the radius of the impactor core is fixed to 500 km and both silicate and iron temperature is fixed to $1300\,K$ (see model *mars2D0* in table 3 and Fig. 13). The accretion history of the planet is compressed into the initial setup, which contains several hundred iron diapirs of 75 km radius (Golabek et al., 2011), corresponding to a planet, which is fully accreted, yet not differentiated. The starting condition is set at a point where the impactor core is already inside the planet, adding a small safety distance between the planets surface and the impactor core to prevent artificial sticking. The planet is surrounded by a sticky air layer, which has a density of $1\,\frac{kg}{m^3}$, constant temperature of $220\,K$ and constant viscosity of $10^{19}\,Pa\,s$. The sticky air will act as a free surface, allowing deformation of the planets surface, while also behaving like an infinite reservoir, absorbing heat released from the planet.
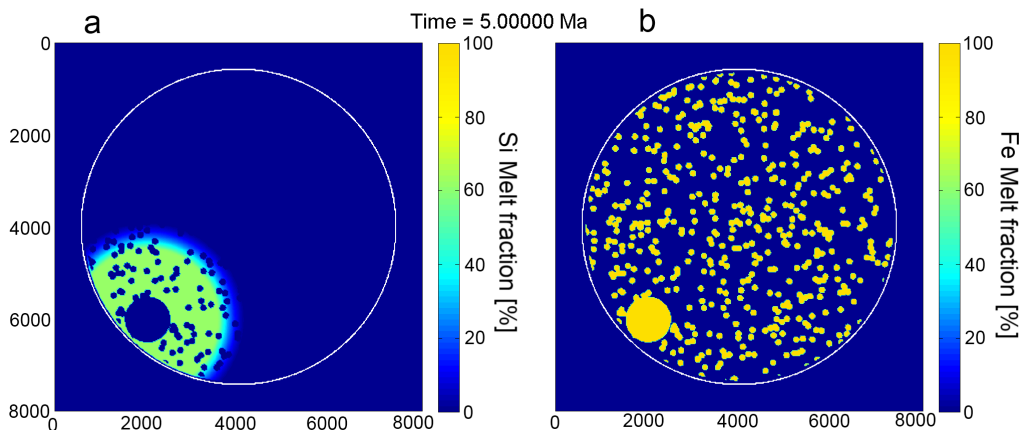

Figure 13: Starting setup of the initial model *mars2D0*. (a) Silicate melt fraction is shown on the left and (b) iron melt fraction is shown on the right. Iron diapirs with radius $75\,km$ are randomly distributed throughout the target body of silicate and the iron impactor core is situated already below the surface.

Compared to the best-fit model by Golabek et al. (2011) a lower value of $300\,ppm\,K$ for the radioactive heating by radiogenic potassium ^{40}K has been chosen for both the solid and liquid iron and silicate phases. This seems to be a more plausible value for planetary bodies (Wänke and Dreibus, 1994). To further map out parameter space, the temperature of both, the iron diapirs, and the impactor core, are varied systematically from $1300\,K$ to $2300\,K$, while the silicate temperature is kept constant at $1300\,K$.

3.2. 3D models

As an initial model for the 3D modelling, an analogue case to the 2D *mars2D0* model has been chosen, as far as this was possible. Initial model *mars3Da0* has an impactor core radius of $464\,km$ and iron and silicate temperature fixed at $1300\,K$ (see table 3 and Fig. 14) . In accordance with the 2D models, the amount of radiogenic potassium ^{40}K has been fixed at $300\,ppm\,K$ for all 3D models as well. The planet is surrounded by sticky air.
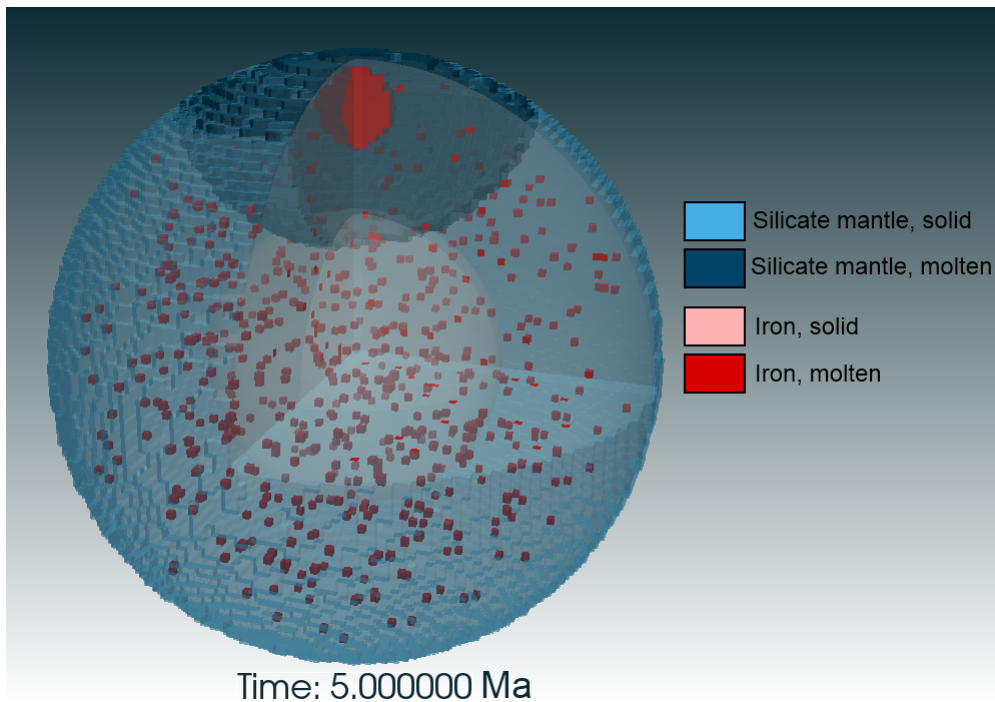

Figure 14: Starting setup of the initial 3D model *mars3D0*. Composition is shown. Iron diapirs with radius $75\,km$ are randomly distributed throughout the target body (indicated in red) of silicate and the iron impactor core is situated already below the surface.

Model *mars3Da0* starts with the setup described in chp. 3.1, with a compressed initial condition. This initial condition is varied in further models *mars3Da1* and *mars3Da2* by setting

the fraction of the target body iron, which still remains in diapirs f_{diap} versus a fraction which has already differentiated into a protocore.

In models *mars3Db1* to *mars3Db4*, like in the 2D models, the temperature of the iron impactor core and the target body iron is varied.

Model *mars3Dc1* acts as a control for model *mars3Db2*, having the same setup but an increased lower Silicate cut-off viscosity of 10^{19} instead of $10^{17}\,Pa\,s$. And finally model *mars3Dd1* is the control for *mars3Db1*, with the same setup but only half the impactor core radius of $232\,km$.

Resolution is chosen at $293 \times 293 \times 293$, which is only about one quarter lower than employed in the 2D models.

4. Results and interpretation in 2D

4.1. Surface magma ocean

Building of crust as discussed in chapter 2.1.7 is not implemented in the 2D code. But in all 2D models impact heat coupled with shear heating produces enough silicate melt to form a hemispherical magma ocean, which spreads out over the planet's surface and is most strongly developed at the impact site (Fig. 15). It then solidifies again in around $10 - 100\,ka$ (Fig. 16c). If crust formation would have been implemented, crust would have been built in the places where Silicate is found close to or at the surface. In this case mostly around the impact site.
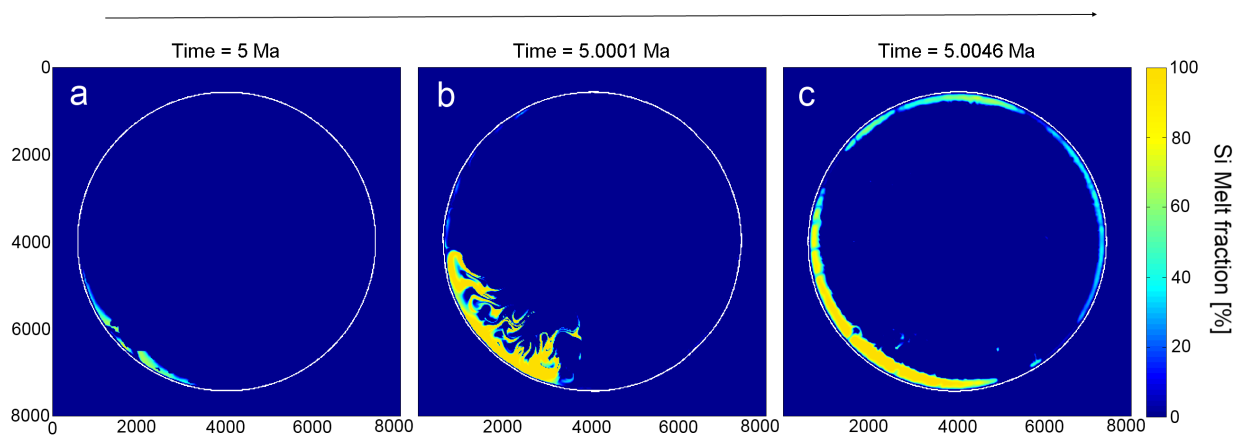

Figure 15: Development of the surface magma ocean in time for the model *mars2D0*. Silicate melt fraction [%] is shown with the impact occurring in the lower left corner.

4.2. Core formation process

In the chosen example *mars2D1* (shown in Fig. 16) a run-away planetary differentiation process (Tonks and Melosh, 1993) can be observed where the impactor core sinks down through the mantle initiating core-mantle differentiation. The impactor core stops somewhere in the depth of the future core-mantle boundary, where it starts pushing against the central region, which has been separated from the mantle by shear heating produced melt (Fig. 16b and c). The central region breaks up along the liquid iron diapir chains, which seem to act as weak zones and the iron assembles in the centre of mass (Fig. 16b). The differentiated planet is left with a hemispherically heterogeneous temperature distribution. At the impact site a thermal anomaly (Fig. 16a) can be observed.
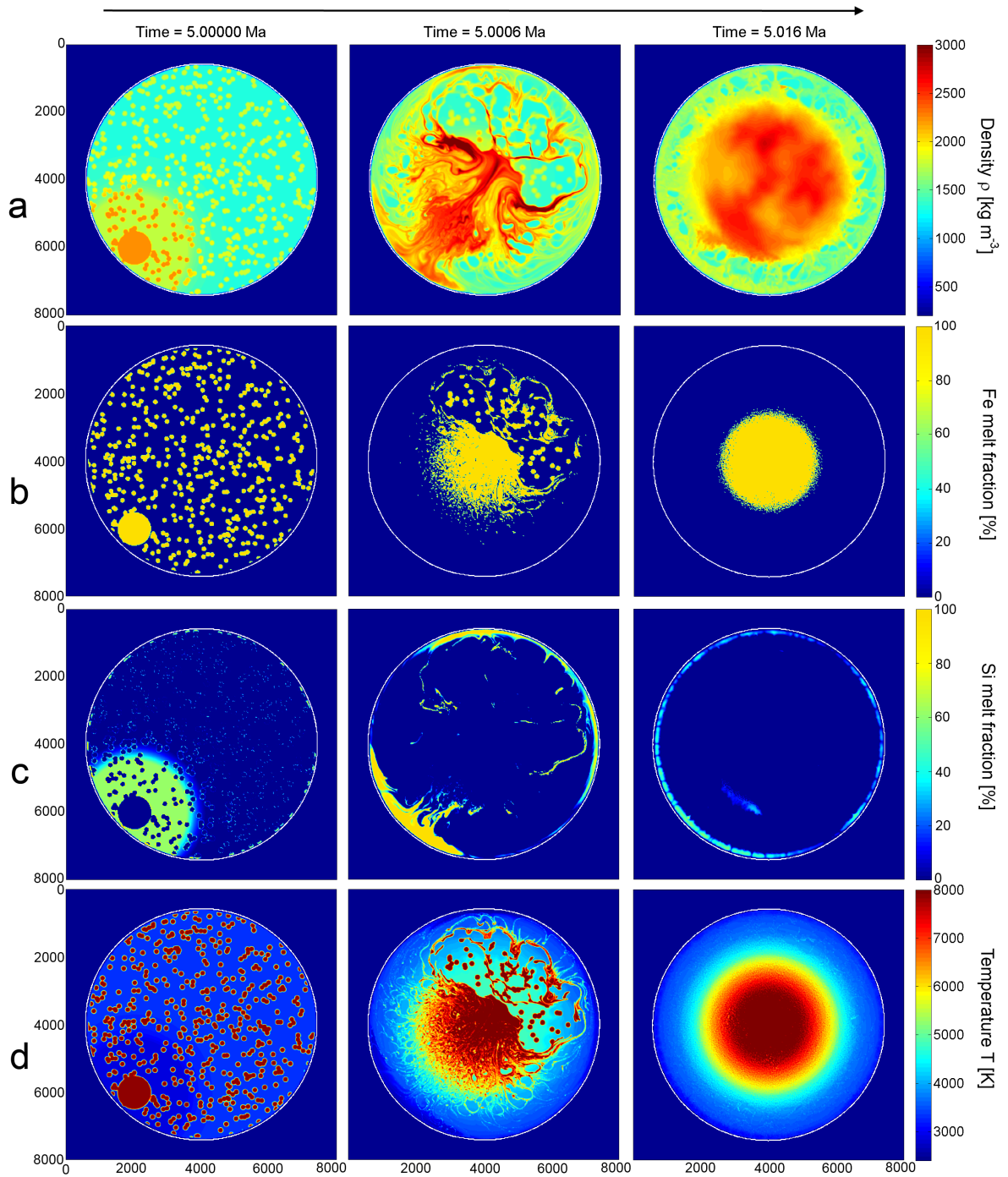
Figure 16: Core formation and development of a thermal anomaly due to the sinking of a giant impactor for the example of model mars2D1. Evolution of (a) temperature, (b) iron melt fraction, (c) silicate melt fraction and (d) density.

4.3. Deep silicate melt pockets

The amount of silicate melt produced at the core-mantle boundary (CMB) varies quite strongly among the different models. Model *mars2D0* shows no silicate melt production at the CMB (Fig. 17a). Most of the models (*mars2D1-mars2D9*, *mars2D11* and *mars2D12*), building a large second group, show a faint trace of a melt pocket below the impact site (Fig. 17b). A third group of models (*mars2D10*, *mars2D13* and *mars2D14*) shows a much larger amount of silicate melt in a nearly continuous layer around the core. Again a large pocket of silicate melt is found below the impact site (Fig. 17c). These differences in silicate melt production mainly result from the mean core temperature (Fig. 18).
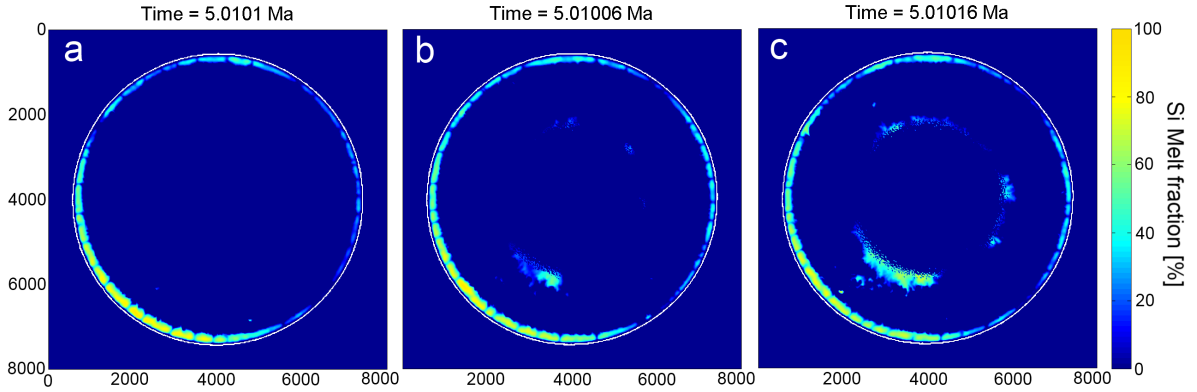

Figure 17: (a) Model *mars2D0* produces no silicate melt at the CMB. (b) A second group, e.g. *mars2D3*, shows a small silicate melt pocket below the impact site and (c) a third group, e.g. *mars2D10* shows a nearly continuous silicate melt layer around the core.

4.4. Influence of temperature variations in iron

Fig. 18 shows roughly two stages in temperature evolution of a model. During the sinking of the impactor and breakup of the central region, temperature rises rapidly due to impact heat and shear heating. After the core is fully differentiated, temperature rises further only very slightly because of radioactive heating and finally, begins to drop.

With increasing initial temperature of the diapirs the breakup of the central region and consequentially, core formation occurs increasingly earlier, as the diapir chains seem to act as weak zones (Fig. 18). Increasing the impactor core temperature instead of the diapir temperature, this effect can be compensated for. Compare for example model *mars2D7* and *mars2D11* in Fig. 19 and Fig. 18. Model *mars2D7*, which has a $200\,K$ hotter diapir temperature is slightly faster with core formation. Though after $200\,ka$ model *mars2D11* with a $1000\,K$

hotter impactor core was able to catch up and both models have the same mean core temperature. Generally the planetary core is formed faster with higher diapir temperature or higher impactor core temperature (Fig. 18).
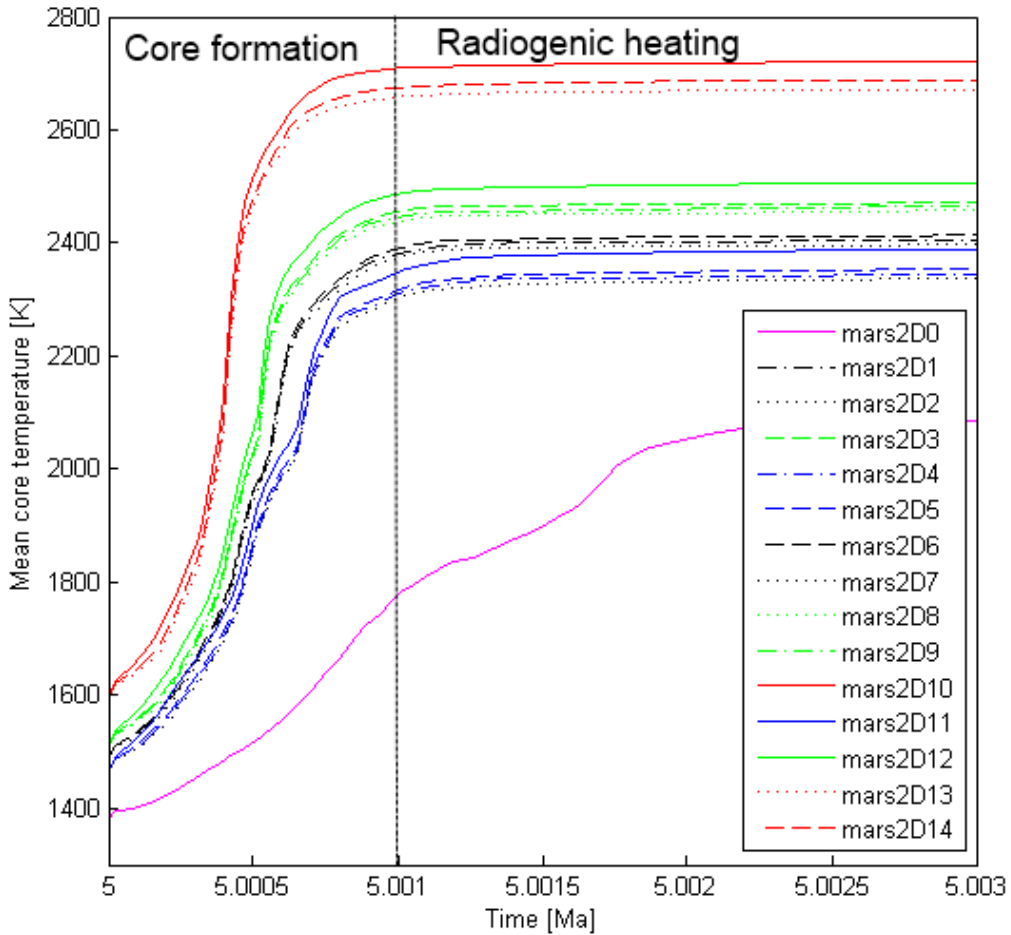

Figure 18: Evolution of the mean core temperature for the investigated 2D models. Two different stages can be clearly observed: Core formation along with a rapid increase in temperature and later radioactive heating.

In the inital model *mars2D0* the final mean core temperature is closest to the final core temperature of $2078\,K$ from the best-fit model done by Golabek et al. (2011) in 2D. In the *mars2D0* model the iron is still solid due to the larger pressure and low temperature in the core. With higher impactor core temperature and higher diapir temperature, the newly formed core gains a higher mean core temperature. Tough it is mainly the diapir temperature, which makes the dominating influence (Fig. 19). This is explained by the larger total mass of the diapirs compared to the impactor core, as the impactor in all models only contains about
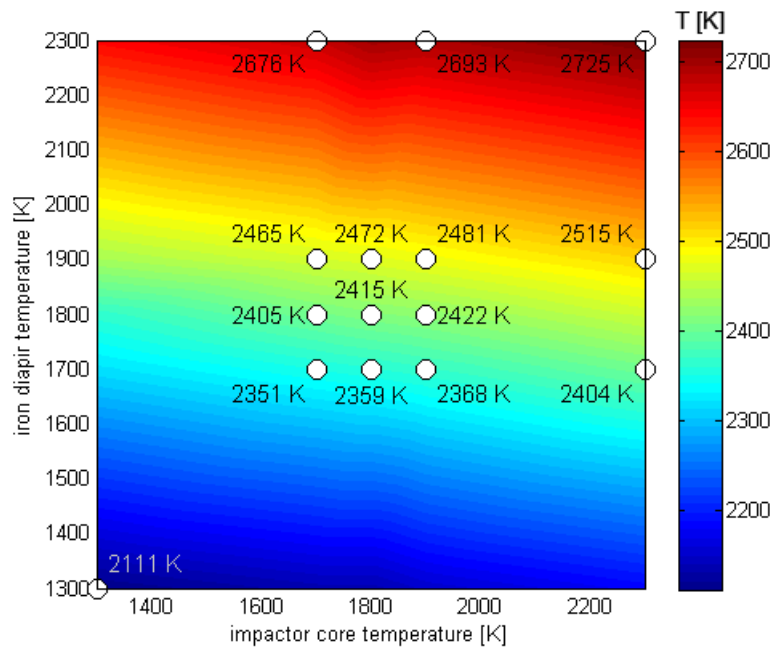
Figure 19: Final mean core temperature of the investigated 2D models after completion of core formation shown in impactor core temperature - diapir temperature space.

8 % of the total iron amount. But hotter iron diapir chains also seem to act as weak zones along which the silicate protocore can break up, thus speeding up, iron core formation.

5. Results and interpretation in 3D

5.1. Crust formation process

A large amount of melt is produced by the impact heat, forming a mushroom shaped cap over the impact site. After a few tens of years crust is already forming and a plume tail is still in development. The impactor core is moving downwards due to negative buoyancy of the iron, taking part of the silicate melt with it and forming the plume tail. See Fig. 20a.

After a few hundred years, downflow in the plume tail seems to have stopped. Positive buoyancy of the silicate melt seems to win out. Most of the crust is at the rim of the developing crustal patch, forming a ring-like structure. See Fig. 20b and c.

In the range of $1000 - 10'000$ years a strong degree-one mantle convection develops. With the plume in the center providing fresh melt continuously, a second inner ring structure develops and crust gets subducted along the whole rim of the spherical, crustal patch. See Fig. 20d and e. Between these two rings a more disturbed pattern can be observed, which probably formed due to convection in crust and mantle. After $\sim 50'000$ years the plume tail becomes weaker, retreating from the CMB. It seems that the plume acted as some kind of anchor, as from now on the crust is moving slowly in random directions, when it was steady before.

Mainly four different types of crust formation have been observed, differing only in details. Crust formation as described above and shown in Fig. 20 leads to a crustal distribution with two strongly distinct, concentric rings and a convective pattern in between (Figs. 21 and 22b). The two rings show up as peaks in a 1D interpolated profile (Fig. 23, though the pattern inbetween is hard to catch in a profile. This type of crust formation can be observed with most of the models, which are starting out with a differentiated protocore: *mars3Da1* and *mars3Db1-mars3Db4*

In the two models which started out undifferentiated (*mars3Da0*) or partially undifferentiated (*mars3Da2*), the diapirs seem to induce additional small scale convection, breaking up the near perfect symmetry in crustal formation (Fig. 22a). Therefore, the 1D profile is more unclear (Fig. 23a).

Mode *mars3Dc1* has an increased lower cut-off viscosity of $10^{19}\,Pa\,s$ for all silicate materials like mantle and crust. This seems to enable crust and mantle to support higher stresses. As in model *mars3Dc1* the crustal patch and surface magma ocean is being pulled down by the impactor far deeper than in reference model *mars3Db2* and reaches almost down to the core (Fig. 35). The following circumference subduction of crust as described above is also missing in this special case.

Model *mars3Dd1* has a smaller impactor core size (Fig. 34d), which mainly results in less impact heat and less silicate melt production. The result is a smaller crust (Fig. 36c) both in extension and thickness.
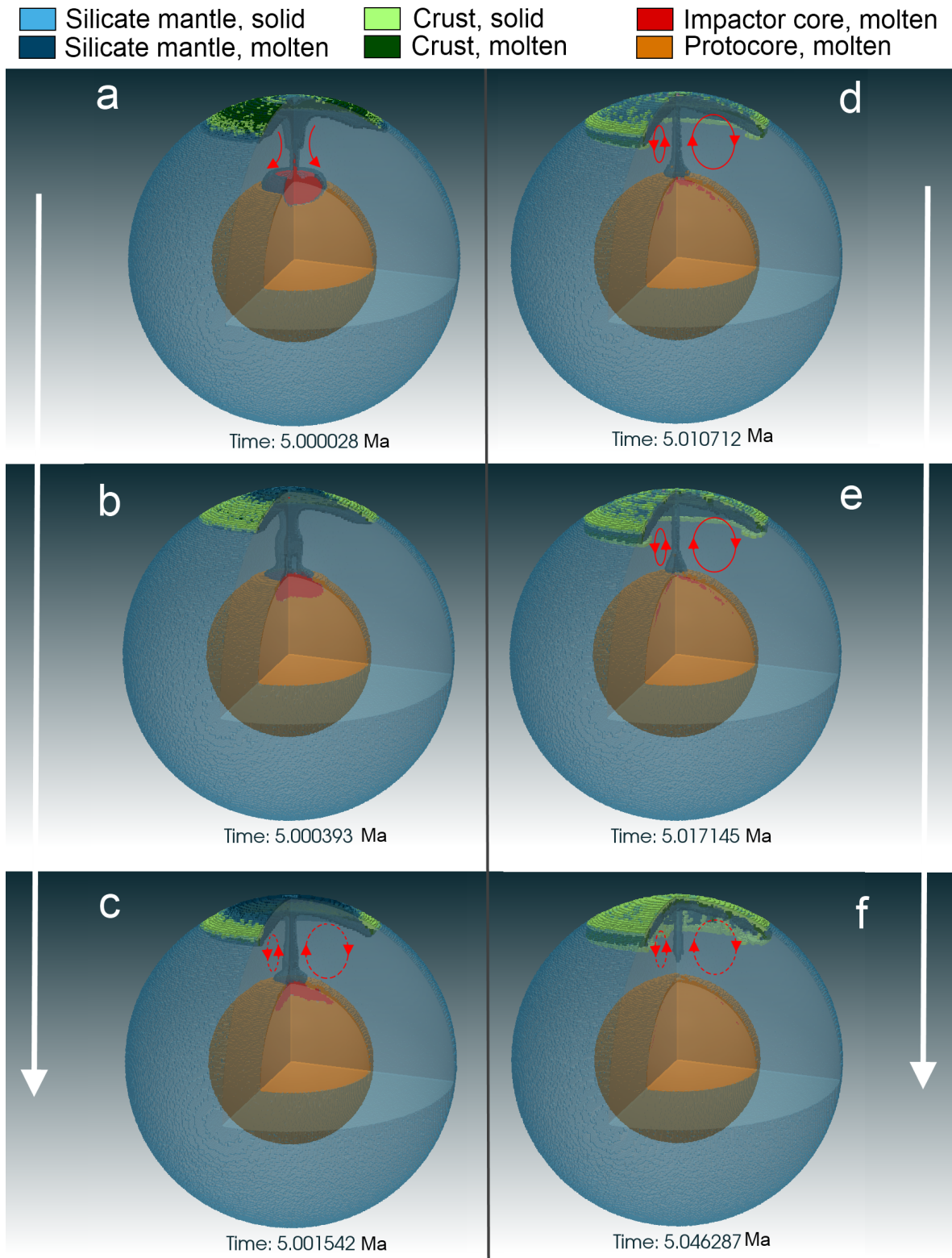
Figure 20: Process of crust formation at the example of model *mars3Db1* advancing in time from (a) to (f). The hypothesised mantle flow is marked with red arrows. Mind the change in mantle flow direction from (a) to (c). In (a) the flow is driven by impact momentum, whereas in (c) it is driven by positive buoyancy.
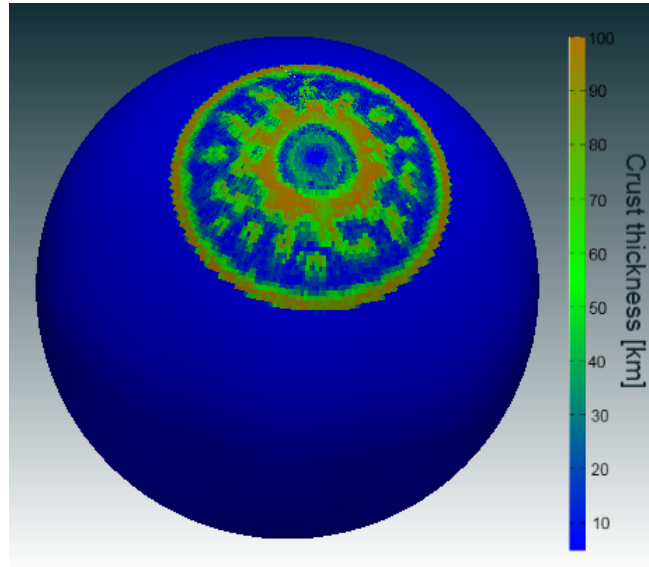
Figure 21: Map of crust thickness for model *mars3Db2* projected onto a sphere. The same crust thickness distribution is shown as in Fig. 22b
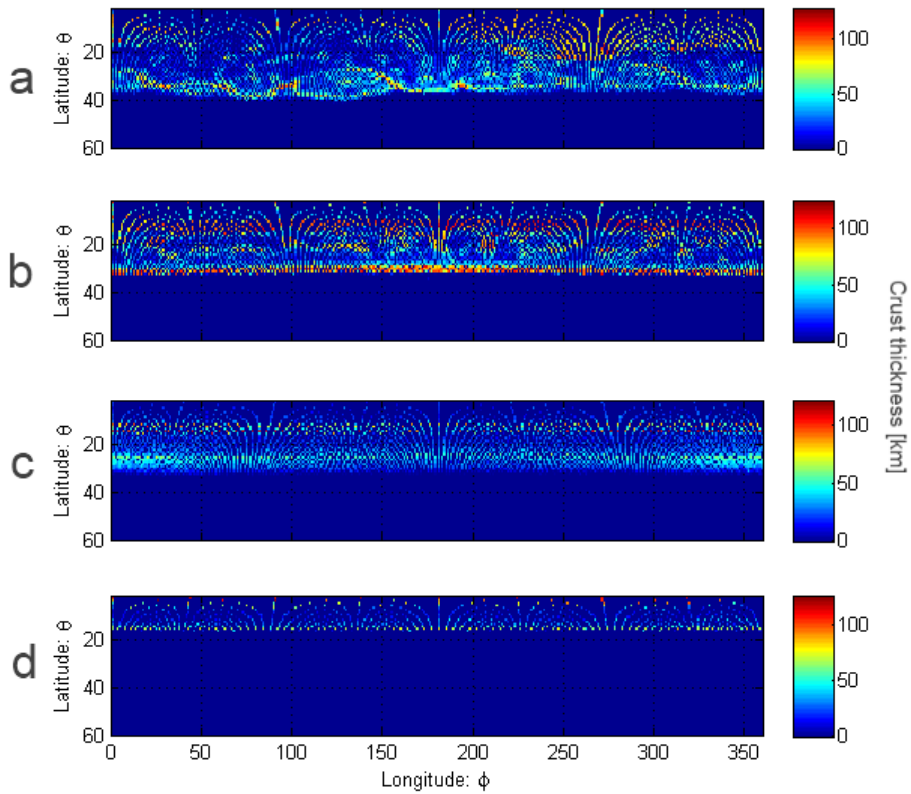

Figure 22: Map of crust thickness for each of the different crustal types shown in Fig.23, represented by models (a) *mars3Da0*, (b) *mars3Db2*, (c) *mars3Dc1* and (d) *mars3Dd1*.
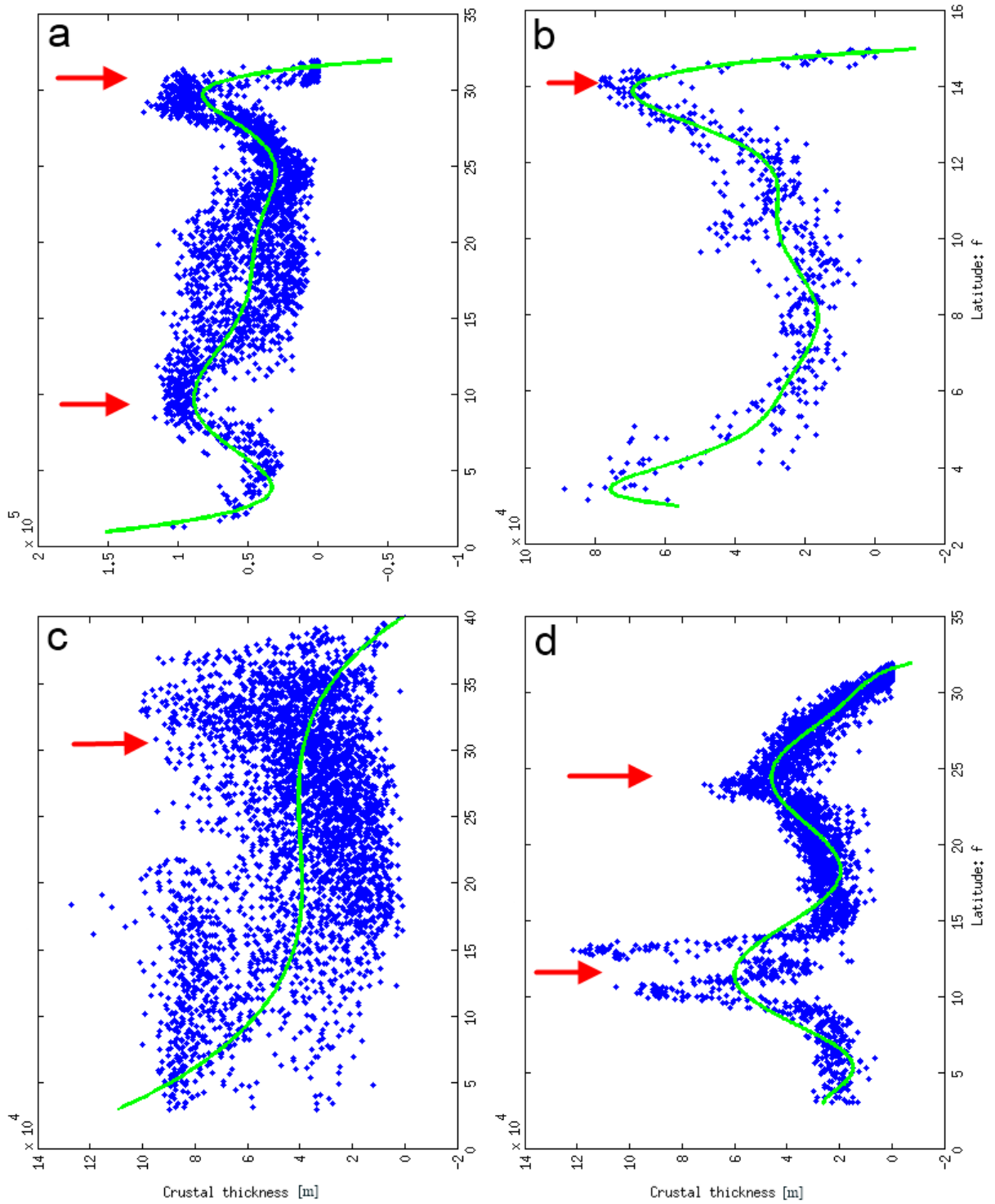
Figure 23: Stacked and interpolated profile for each of the different crustal types shown in Fig.22 represented by models (a) *mars3Da0*, (b) *mars3Db2*, (c) *mars3Dc1* and (d) *mars3Dd1*. The location of strong features is marked with red arrows.

5.2. Core formation: Liquid outer core or deep magma ocean?

One mode of core formation is mainly seen in models with already predifferentiated core (*mars3Da1*, *mars3Da2*, *mars3Db2* and *mars3Dc1*). The hot, liquid impactor core sinks through the mantle and when it hits the solid protocore, it cannot penetrate (Fig. 24a). Impact momentum coupled with the positive buoyancy of the hotter, molten impactor, forces it to spread around the CMB (Fig. 24b). On its way around the core, the impactor iron starts to melt the uppermost layer of the iron protocore (Fig. 24c). After around $500'000$ years the whole core is covered by an outer layer of liquid iron (Fig. 24d).

The iron of the former impactor core is now wide spread in the outer, liquid iron layer. But the new outer core is mainly formed from molten protocore material as can be seen in both Figs. 25a and b. At the antipode of the impact on the core surface, there is also impactor material frozen into the new, solid inner core (Figs. 25a and b). But in contrary to the Earths two-layered core, the inner, solid layer is cooler than the outer layer (Fig. 26).

This model of creating a liquid, outer core by giant impact, has already been proposed by (Reese and Solomatov, 2010). Reese and Solomatov (2010) suggested that a minimal thickness of the outer layer of $10 - 30\,km$ would be necessary at least, to support a dynamo. All models with inner and outer core have an outer core layer thickness of $200 - 400\,km$ and would therefore allow dynamo action. Existence of a dynamo can be estimated by means of the magnetic Reynolds number Re_M, which should exceed a lower critical value $Re_{M,cr}$ 10 (Reese and Solomatov, 2010),

$$Re_M = \frac{v_c z_c}{\mu_0 \sigma} > Re_{M,cr}\ 10, \tag{5.1}$$

where v_c is the convective velocity, z_c is the layer thickness, μ_0 is the permeability of free space and σ is electrical conductivity.

This model would suggest an excellent way of creating a dynamo, which can be shut off easily, fulfilling the requirement of present day Mars having no active dynamo (Acuña et al., 1999).

In a second mode of core formation, the impactor is able to penetrate through the protocore (Fig. 27a) and impactor core iron and parent body iron start to mix (Fig. 27b). This can only happen if the temperature of the impactor at the CMB is lower or nearly the same as the protocore. It allows the impactor to travel through the protocore as well and, after equilibrating, to mix with the protocore material.

Due to the high mean temperature of the final core, silicate material at the core-mantle boundary is molten and forms small melt pockets (models *mars3Da0* and *mars3Db3*) and in
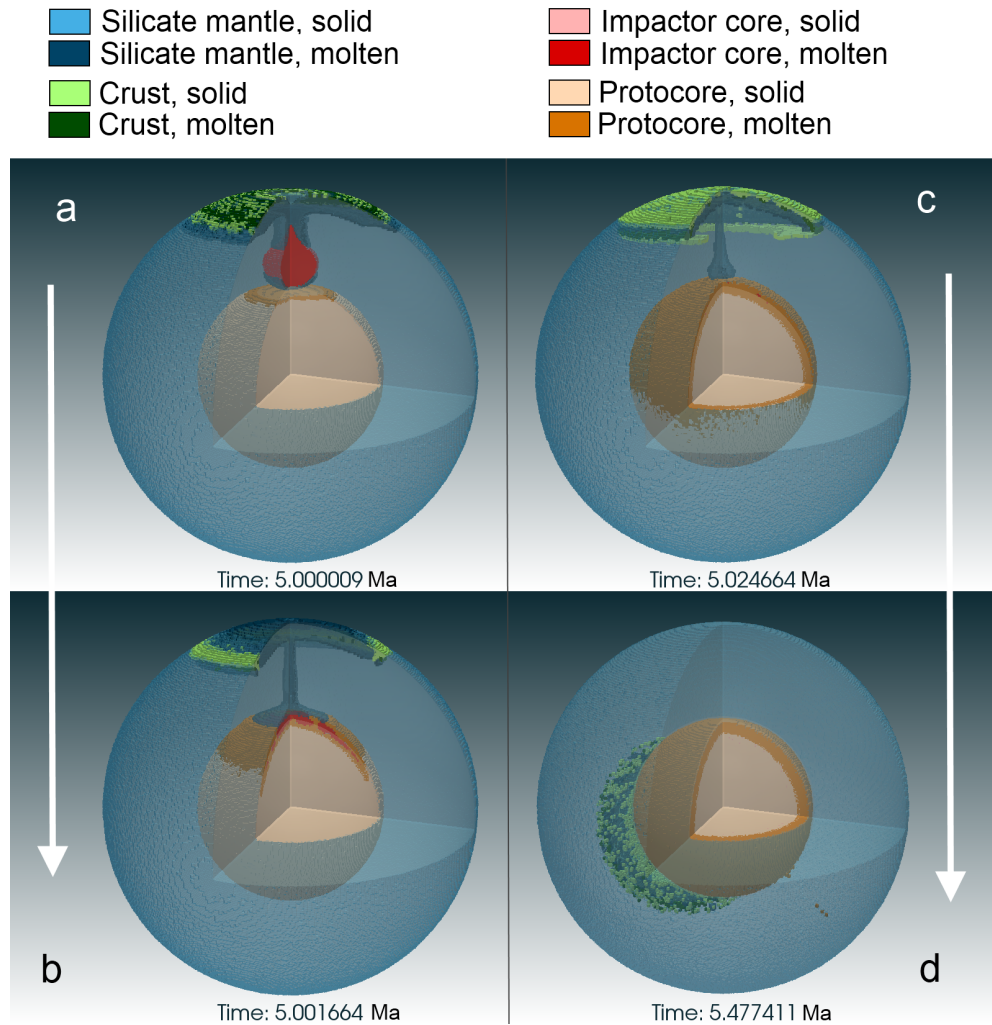
Figure 24: Formation of molten, outer core shown by the example of model *mars3Db2*. (a) The impactor core is molten, while the predifferentiated core of the target body is still solid. (b)-(c) The impactor core cannot penetrate the protocore, but instead starts to melt its way along the core-mantle boundary. (d) After about 500′000 years the still solid protocore is fully surrounded by molten iron.

the case of the model with highest mean core temperature *mars3Db4* (table 5) larger melt pockets or a nearly continuous silicate melt layer around the core, in stark contrast to the core formation mode described above, where an additional layer of liquid iron is formed around the protocore.

There is also a transitional mode, where the impactor core cannot penetrate the protocore because of its positive buoyancy, even though both are liquid. The resulting core is fully molten, bus has an outer layer of impactor core iron (Fig. 28) distinguished by its slightly lower density.
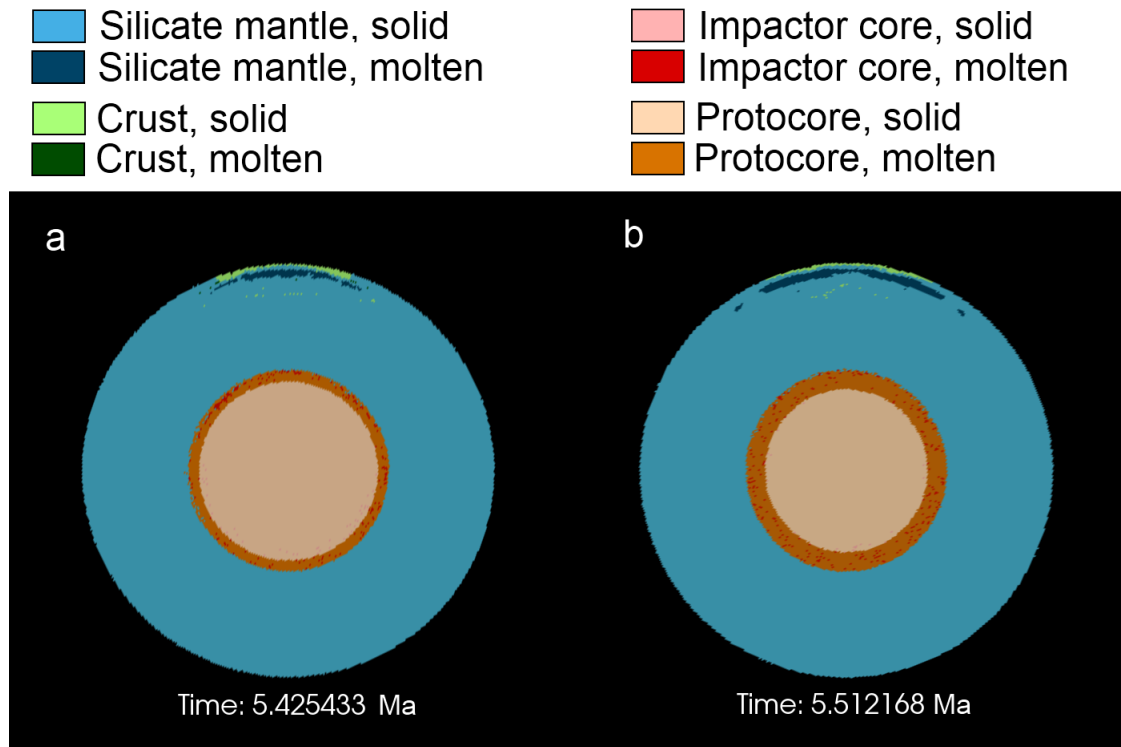
Figure 25: Solid inner core and liquid outer core shown for models (a) *mars3Db2* and (b) *mars3Dc1*.
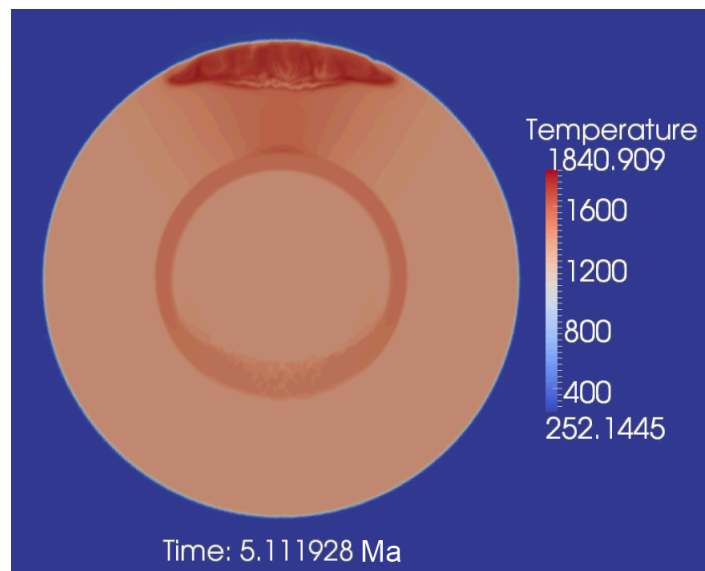

Figure 26: Solid inner core and liquid outer core shown for model *mars3Db2*. The solid, inner core is not only solid due to larger pressure, but mostly due to lower temperature. The liquid outer core is mainly a thin hot layer surrounding the cooler, inner core.

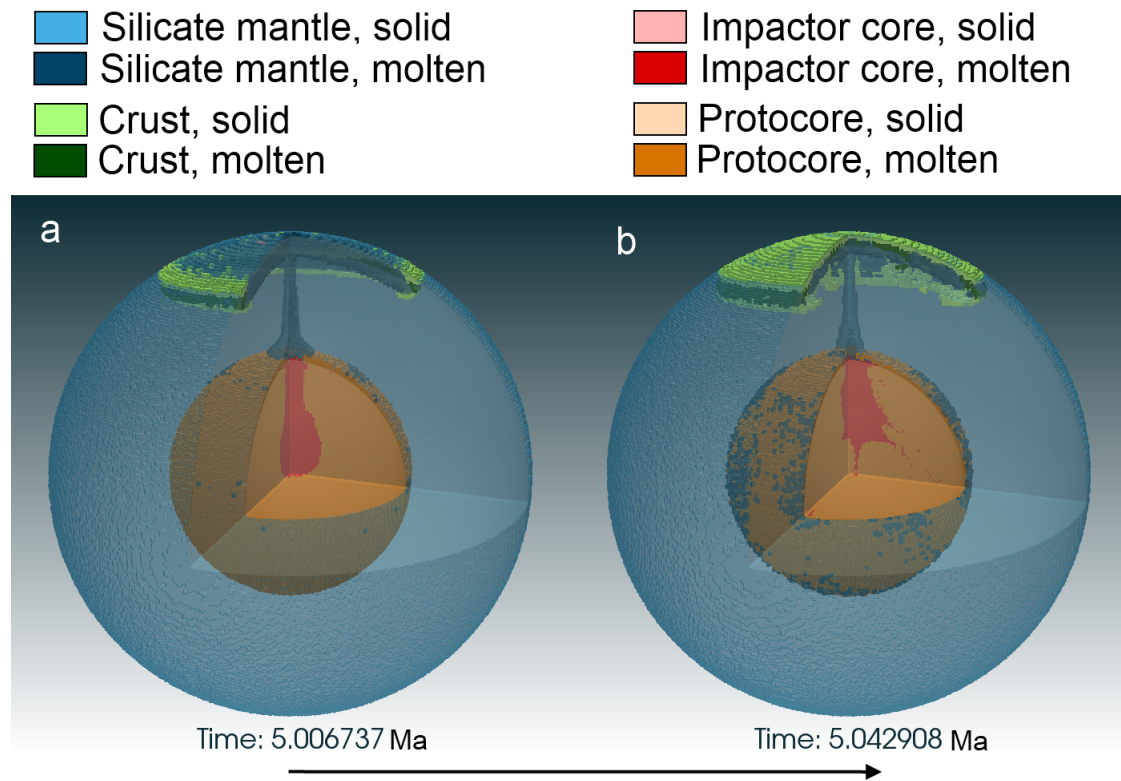Figure 27: Core formation for a hot protocore and cool impactor (*mars3Db4*). (a) This combinations will allow the impactor to penetrate the protocore and (b) after equilibrating to mix with protocore iron.
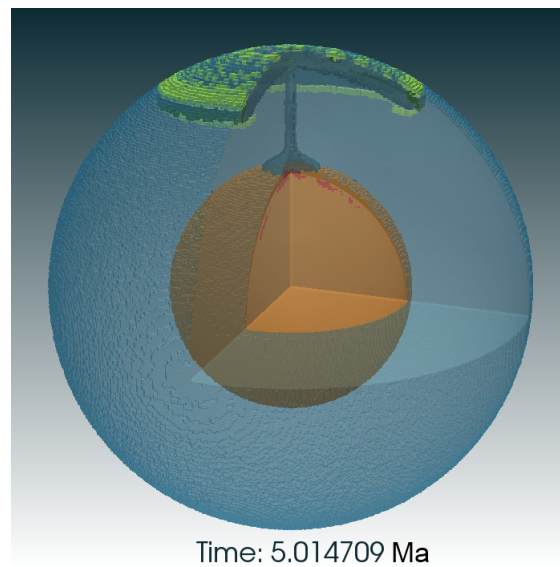

Figure 28: Model *mars3Db3* shows a transitional state between the two proposed core formation modes. The impactor cannot penetrate the protocore, but no differentiation into solid inner and liquid outer core happens.

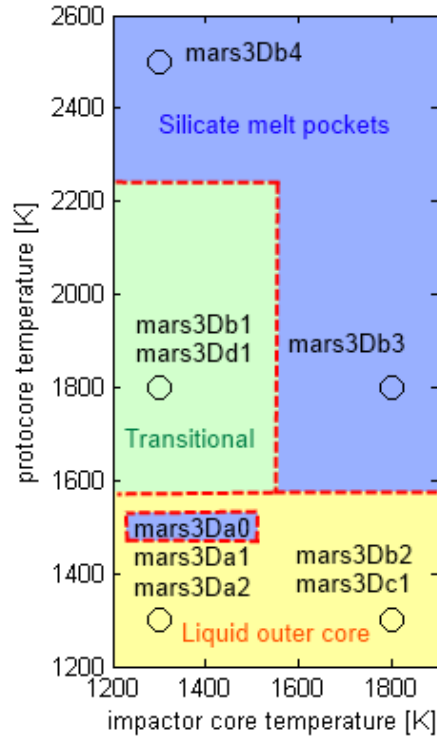## 5.3. Influence of temperature variations in iron

Figure 29: The mode of core formations mainly depends on temperature. Initial protocore or diapir temperature is plotted against initial impactor core temperature for each 3D model.

Which of the above described core formations modes takes place, mainly depends on the temperature of the target body iron (diapirs, protocore or both). In the case of a cold protocore or diapirs of $1300\,K$, the temperature seems to have no influence. The impactor core heats up due to impact heat and shear heating, such that even an impactor which starts out with the same $1300\,K$ will be hot enough when it reaches the protocore, that it is positively buoyant and forms a liquid outer core layer, with the cold solid protocore as new inner core (see Fig. 29 'Liquid outer core'-mode marked in yellow). In the case of diapirs involved this is slightly different, as the diapirs themselves add heat to the final core after merging with it.

If the final mean core temperature is hot enough, silicate material at the core-mantle boundary is molten and forms melt ponds or a silicate layer around the core (see Fig. 29 'Silicate melt pockets'-mode in blue).

If the final mean core temperature is not high enough to melt the silicates at the CMB but the core is still not differentiated in solid inner and liquid outer core, this mode is labelled 'Transitional' in Fig. 29 and marked green.
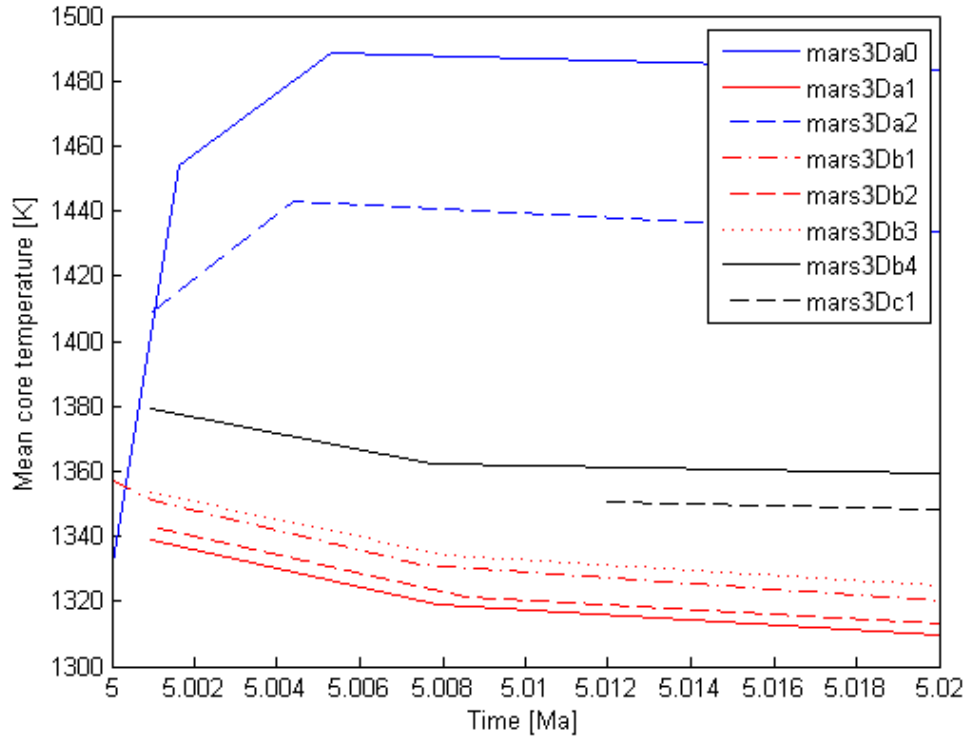
Figure 30: Mean temperature of the future core region for all of the 3D models.

The impactor core temperature has only a very small effect on the core formation process (Fig. 31, which is easily explicable as the impactor core only contains about 3% of the total iron mass.

5.4. Diapir vs differentiated setup

The only difference between models *mars3Da0*, *mars3Da1* and *mars3Da2* is, how the same amount of target body iron is distributed between diapirs and protocore, modelling degree of differentiation. Model *mars3Da0* starts out with only diapirs (Fig. 34a), model *mars3Da1* starts out with only a protocore (Fig. 34c) and model *mars3Da2* begins with half of the mass of target body iron in randomly distributed diapirs and the other half in the protocore (Fig. 34b).

Both mantle and core in the two models with diapirs are $\sim 200\,K$ hotter. The temperature difference between the two diapir models is very small; the undifferentiated model with only diapirs is $50\,K$ hotter than the half-differentiated model. This temperature difference can be explained with the heating due to conversion of gravitational potential energy.
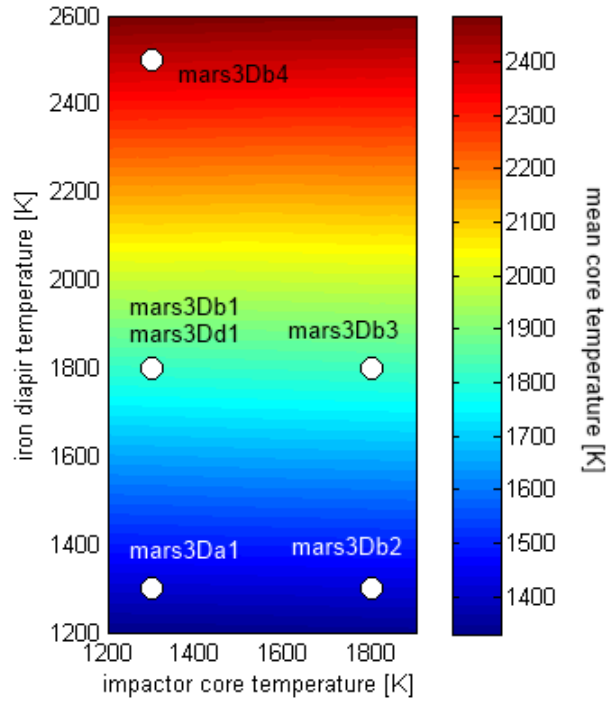
Figure 31: Mean core temperature distribution of models *mars3Da1* and *mars3Db1-mars3Db4* shown in initial impactor core temperature versus initial protocore temperature space.

Diapirs seem to add a component of chaos and small scale convection, as already discussed in chapter 5.1. This might lead to a spatially more variable mantle and stimulate initiation of mantle convection.

On the other hand the here proposed giant impact happens late in planetary accretion history. Current understanding indicates that differentiation started almost immediately after accretion commenced (Chambers, 2004). It is therefore more likely that by the time the giant impact happens, the planet is at least partially differentiated as it is for example in model *mars3Da2*.

6. Comparison: 2D vs 3D

6.1. Scaling considerations

The major difference between the 2D and the 3D models lays in the scaling. In the 2D models the planet appears only as a circle, which is modelled as a infinitely long cylinder. In contrast to the 3D model, where the planet is modelled as a sphere.

If the core radius $r_p = 0.5R_{Mars}$, where R_{Mars} is the total planet radius, then the relative volume occupied by the core in 3D is,

$$f_{c,vol} = \frac{\frac{4}{3}\pi r_p^3}{\frac{4}{3}\pi R_{Mars}^3} = 0.5^3 = 0.125, \tag{6.1}$$

In 2D the relative area occupied by the core is the following,

$$f_{c,area} = \frac{\pi r_p^2}{\pi R_{Mars}^2} = 0.5^2 = 0.25, \tag{6.2}$$

Therefore, if the core is assumed to consist mainly of iron, the 2D model contains more iron.

For an impactor core radius of $500\,km$ or $r_{ic} = 0.15R_{Mars}$, the volume fraction of iron, contained in the impactor, compared to the total volume of iron, is the following,

$$f_{i,vol} = \frac{\frac{4}{3}\pi r_{ic}^3}{\frac{4}{3}\pi r_p^3 + \frac{4}{3}\pi r_{ic}^3} = \frac{0.15^3}{0.5^3 + 0.15^3} \approx 3\%, \tag{6.3}$$

In 2D the relative area occupied by the impactor core compared to the total area occupied by iron is the following,

$$f_{i,area} = \frac{\pi r_{ic}^2}{\pi r_p^2 + \pi r_{ic}^2} = \frac{0.15^2}{0.5^2 + 0.15^2} \approx 8\%, \tag{6.4}$$

This means that the effect of the impactor core, which is relatively small in 2D, is even smaller in 3D for the core size chosen.

And finally for the total iron amount made up by the impactor core r_{ic} and the target body iron r_p, the total volume fraction of iron, compared to the total planetary volume is,

$$f_{i,vol} = \frac{\frac{4}{3}\pi r_p^3 + \frac{4}{3}\pi r_{ic}^3}{\frac{4}{3}\pi R_{Mars}^3} = 0.5^3 + 0.15^3 \approx 13\%, \tag{6.5}$$

The total area fraction of iron in 2D compared to the planetary area is,

$$f_{i,area} = \frac{\pi r_p^2 + \pi r_{ic}^2}{\pi R_{Mars}^2} = 0.5^2 + 0.15^2 \approx 27\%, \tag{6.6}$$

Those effects have to be given thought to when comparing 2D and 3D data.

6.2. Crust formation

The version of the 2D code I2ELVIS used here does not produce any crust. But if it would have been implemented, crust would have been produced most probably in a similar way as in the 3D models. In both 2D and 3D a large magma pond is produced at the surface by the impact. New crust is produced around the impact site, forming a thick crustal patch symmetric to the impact site.

Surface magma production is much more energetic in most 2D models compared to 3D but this is explained by the generally higher temperature of all 2D models, as only diapirs are used as initial setup.

In both 2D and 3D the crust (or in 2D the silicate melt pond) start to move away from the impact site in a seemingly random direction as soon as the plume detaches from the core.

6.3. Core formation

Only one of the two core formation styles introduced in chapter 5.2 can be observed in the 2D models. The reason is the generally higher temperature of all 2D models, which do not allow a solid inner core, but are in most cases high enough to produce melt pockets or in one case a nearly continuous silicate melt layer. But these silicate melt pockets can only be observed in two cases in 3D models, where the parent body iron is hot enough to melt silicate material close to the core-mantle boundary. The double layer magma ocean which has been observed for high mean core temperatures is consistent with similar studies, also done for the Earth (Labrosse et al., 2007).

The liquid outer core mode though, cannot be observed in any of the 2D models. It is consistent with results from Reese and Solomatov (2010).
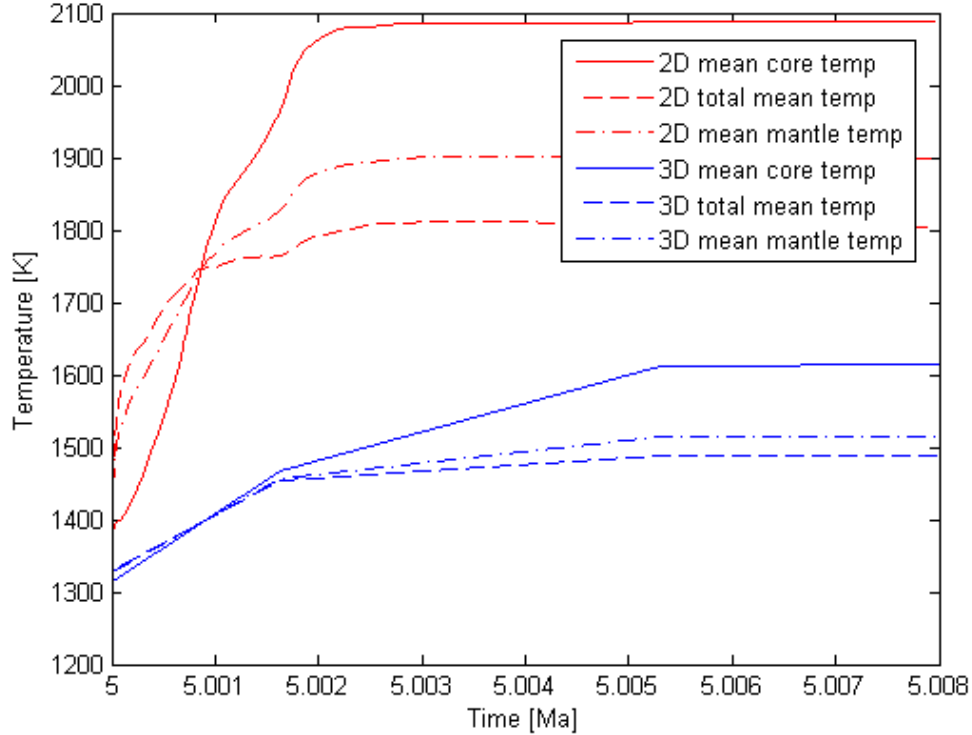
6.4. Influence of temperature variations in iron

Figure 32: Mean temperature of the future core region for each of the 3D models.

In the inital 2D model *mars2D0* the final mean core temperature is closest to the $2078\,K$ from the best-fit model by Golabek et al. (2011). But all 2D models have a total mean temperature up to $700\,K$ higher. The main difference is the higher iron temperature in both target body iron and impactor core to compensate for the decreased heating by radiogenic potassium ^40K.

In 3D models the mean core temperature is generally $500\,K$ lower than in the 2D models. There are two reasons for this. Most 3D models had a start setup with an already differentiated protocore compared to the 2D models which all started with the diapir setup. As already discussed above (chp. 5.4), the differentiation of the diapir setup releases some additional heat, which leads to a higher mean core temperature. But if this would be the only reason, then the 3D model *mars3Da0*, which started out with a diapir setup as well, would need to be in the same range with its mean core temperature as its equivalent 2D model *mars2D0* (Fig. 32). The 3D model still has a mean core temperature of $\sim 500\,K$ lower, which can be explained by scaling from 2D to 3D. The 2D models have an area of $\sim 27\%$ of iron in total, whereas, the 3D models only have a volume of $\sim 13\%$ of iron, even if the same radii for impactor core, protocore and diapirs are used.

With higher impactor core temperature and higher diapir or protocore temperature, the newly formed core gains a higher mean core temperature. Tough it is the temperature of the target body iron, which makes the dominating influence (Figs. 19 and 31). This is explained by the larger total mass of the diapirs and the protocore compared to the impactor core, as the impactor core in all 2D models only contains about 8% of the total iron amount. In the 3D models, this fraction is even smaller and the impactor core contains only $\sim 3\%$ of the total iron, making nearly no difference.

6.5. Best-fit model

A good criterion for a best-fit model would be the ability to generate a dynamo. Dynamo generation is not shown for any of the models in 2D and 3D, but is possible for all models, which have a liquid outer core of thickness larger than $10 - 30\,km$ (Reese and Solomatov, 2010).

Chosen as best-fit model here is therefore, the 3D model *mars3Da2*, which joins diapir with differentiated setup, seemingly the most realistic, but still benefiting from the advantages of the diapir setup: Easy convection initiation and more variable mantle convection.

The solid inner core is formed from the protocore, the liquid outer core is formed from the diapirs, which are heated up during their decent through the mantle. The crustal patch is somewhat irregular shaped and not totally symmetric, due to the influence of the diapirs.
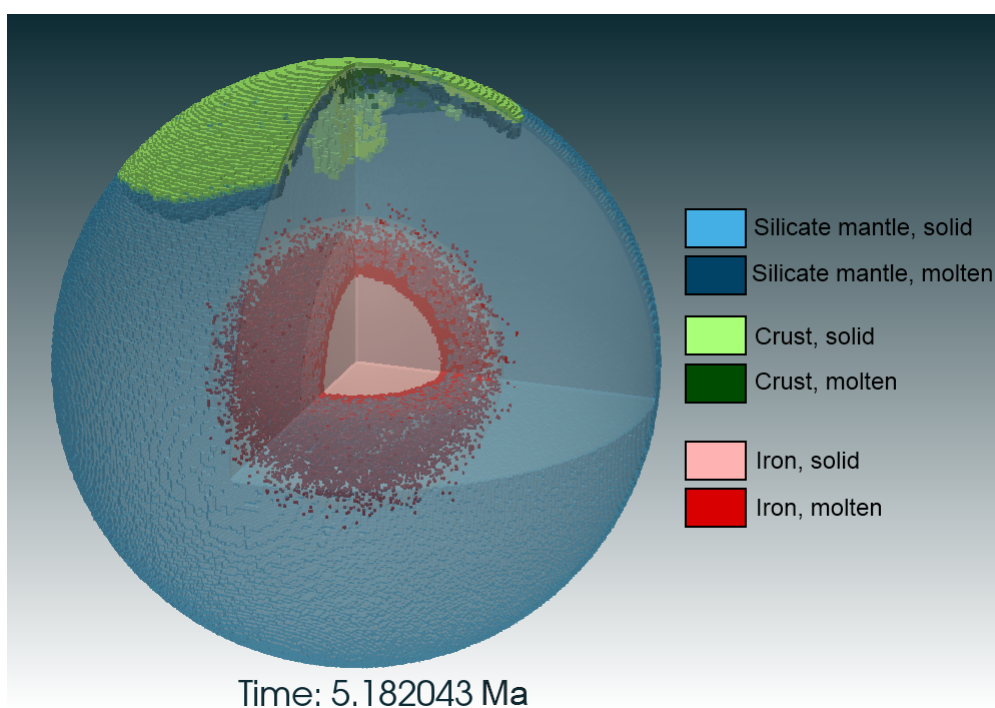
Figure 33: Best-fit model *mars3Da2* started from a half-diapir and half-protocore setup (Fig. 34). The formed crust is somewhat irregular, due to the induced small scale convection by the diapirs, and the core is differentiated into a solid inner and a liquid outer core.

7. Conclusion & Outlook

In this thesis I was able to investigate the influence of the initial thermal condition for the iron and different initial setups on the process, which both occurred to be an important parameter controlling further planetary evolution. To support lower values of radiogenic isotopes, higher impactor core temperature or higher temperature in the target body iron, in this case diapirs or a predifferentiated protocore, are needed. Diapirs or protocore though, are much more efficient in raising mean core temperature due to the iron mass balance.

For generally lower temperatures, but high impactor core temperature, I was able to show, that the hot impactor core lays itself around the cold protocore as predicted by Reese and Solomatov (2010), forming a liquid, outer core layer. If this outer core becomes thick enough, which was the case in all models with a differentiated core, it can support a dynamo. This presents an easy mechanism of starting and then shutting off again a dynamo.

Acknowledgement

References

Acuña, M. H., Connerney, J. E. P., Ness, F. N., Lin, R. P., Mitchell, D., Carlson, C. W., McFadden, J., Anderson, K. A., Rème, H., Mazelle, C., Vignes, D., Wasilewski, P., and Cloutier, P. (1999). Global distribution of crustal magnetization discovered by the mars global surveyor mag/er experiment. *Science*, 284(5415):790–793.

Albers, M. (2000). A local mesh refinement multigrid method for 3-d convection problems with strongly variable viscosity. *Journal of Computational Physics*, 160(1):126–150.

Chambers, J. E. (2004). Planetary accretion in the inner solar system. *Earth and Planetary Science Letters*, 223(3-4):241–252.

Duretz, T., May, D. A., Gerya, T. V., and Tackley, P. J. (2011). Discretization errors and free surface stabilization in the finite difference and marker-in-cell method for applied geodynamics: A numerical study. *Geochem. Geophys. Geosyst.*, 12(7):Q07004.

Frey, H. V. (2006). Impact constraints on the age and origin of the lowlands of mars. *Geophysical Research Letters*, 33(8).

Gerya, T. V. (2010). *Introduction to Numerical Geodynamic Modelling*. Cambridge University Press.

Gerya, T. V., Duretz, T., and May, D. A. (in prep). A hierarchical based adaptive staggered grid, finite difference discretisation for variable viscosity stokes flow and geodynamic modelling - i: Methodology and verification.

Gerya, T. V. and Yuen, D. A. (2003). Characteristics-based marker-in-cell method with conservative finite-differences schemes for modeling geological flows with strongly variable transport properties. *Physics of the Earth and Planetary Interiors*, 140(4):293–318.

Gerya, T. V. and Yuen, D. A. (2007). Robust characteristics method for modelling multiphase visco-elasto-plastic thermo-mechanical problems. *Physics of the Earth and Planetary Interiors*, 163(1-4):83–105.

Golabek, G. J., Keller, T., Gerya, T. V., Zhu, G., Tackley, P. J., and Connolly, J. A. D. (2011). Origin of the martian dichotomy and tharsis from a giant impact causing massive magmatism. *Icarus*, 215(1):346–357.

Labrosse, S., Hernlund, J. W., and Coltice, N. (2007). A crystallizing dense magma ocean at the base of the earth's mantle. *Nature*, 450(7171):866–869.

Mishin, Y. A., Gerya, T. V., Vasilyev, O. V., and Burg, J.-P. (2010). *A wavelet-based adaptive finite element method for the Stokes problems.* PhD thesis.

Monteux, J., Coltice, N., Dubuffet, F., and Ricard, Y. (2007). Thermo-mechanical adjustment after impacts during planetary growth. *Geophys. Res. Lett.*, 34(24):L24201.

Reese, C. C. and Solomatov, V. S. (2010). Early martian dynamo generation due to giant impacts. *Icarus*, 207(1):82–97.

Revenaugh, J. and Parsons, B. (1987). Dynamic topography and gravity anomalies for fluid layers whose viscosity varies exponentially with depth. *Geophysical Journal of the Royal Astronomical Society*, 90(2):349–368.

Rubie, D. C., Nimmo, F., and Melosh, H. J. (2007). Formation of earth's core. In Editor-in Chief: Gerald, S., editor, *Treatise on Geophysics*, pages 51–90. Elsevier, Amsterdam.

Schmid, D. W. and Podladchikov, Y. Y. (2003). Analytical solutions for deformable elliptical inclusions in general shear. *Geophysical Journal International*, 155(1):269–288.

Senshu, H., Kuramoto, K., and Matsui, T. (2002). Thermal evolution of a growing mars. *J. Geophys. Res.*, 107(E12):5118.

Tonks, W. B. and Melosh, H. J. (1993). Magma ocean formation due to giant impacts. *Journal of Geophysical Research-Planets*, 98(E3):5319–5333.

Watters, T. R., McGovern, P. J., and Irwin Iii, R. P. (2007). Hemispheres apart: The crustal dichotomy on mars. *Annual Review of Earth and Planetary Sciences*, 35(1):621–652.

Wänke, H. and Dreibus, G. (1994). Chemistry and accretion history of mars. *Philosophical Transactions of the Royal Society of London Series a-Mathematical Physical and Engineering Sciences*, 349(1690):285–293.

A. Appendix
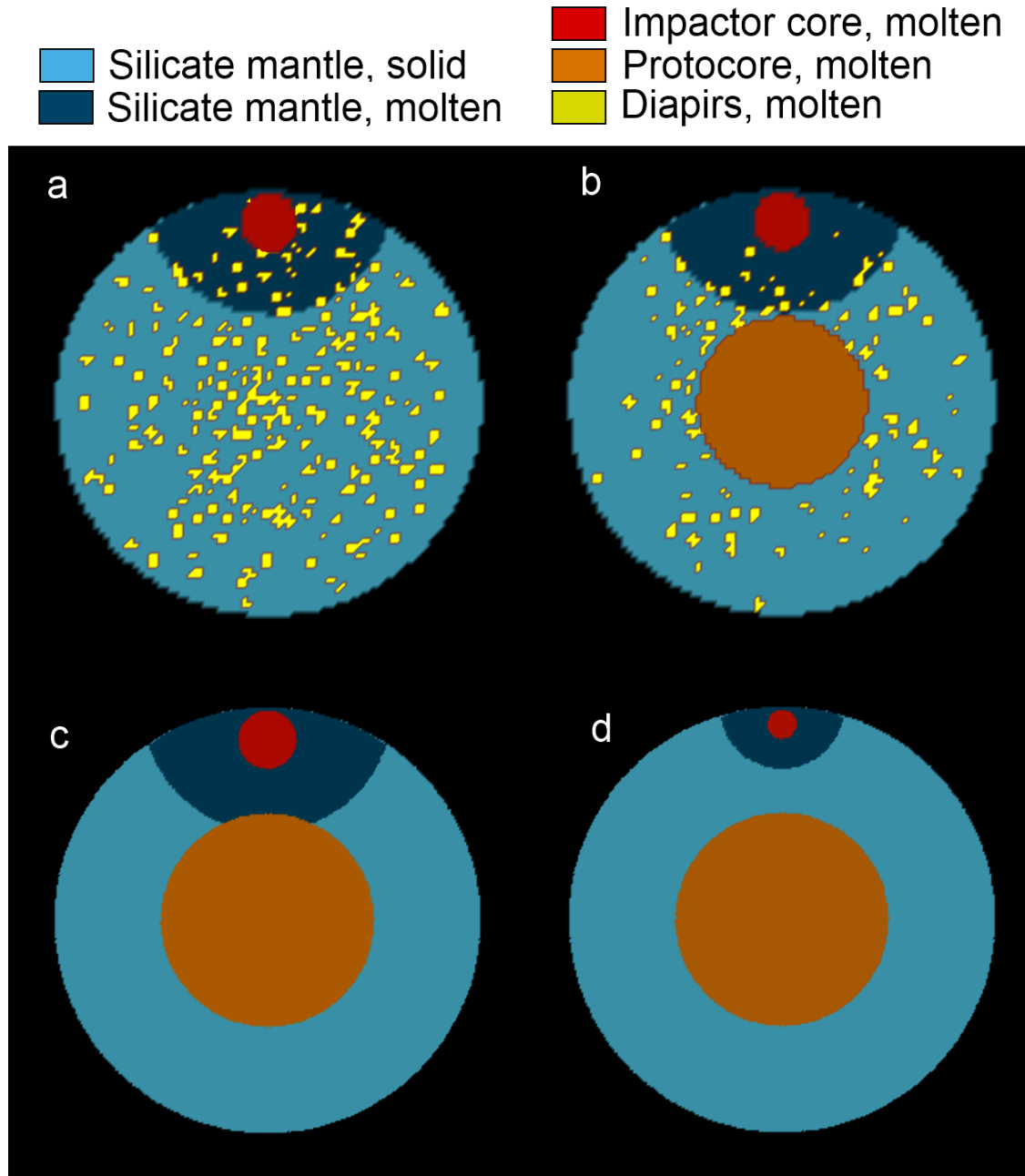
Figure 34: All four different initial setups for the 3D models shown as 2D slices displaying composition. (a) Model *mars3Da0* has only iron diapirs and has the same setup as the 2D models. (b) Model *mars3Da2* has half of its target body iron mass in diapirs and the other half in the protocore. (c) Models *mars3Da1*, *mars3Db1-mars3Db4* and *mars3Dc1* have only a protocore and (d) model *mars3Dd1* has an impactor core of only half the size compared to all other models.
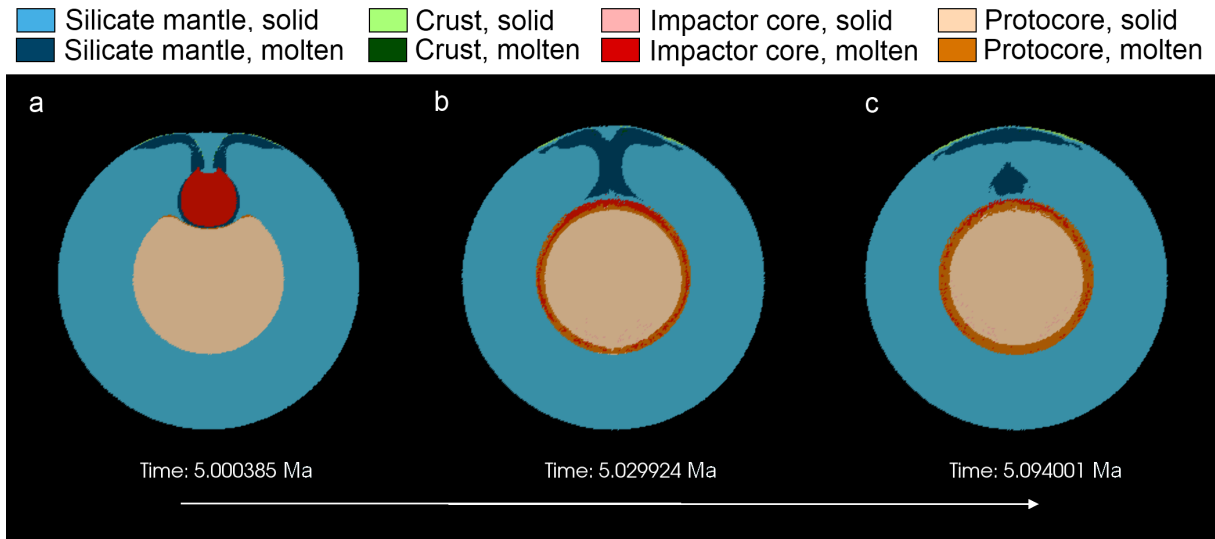
Figure 35: Crust and core formation for model *mars3Dc1* with an increased lower cut-off viscosity of $10^{19}\,Pa\,s$. Shown are slices through the 3D composition model. (a) A higher cut-off viscosity seems to make it possible to support higher stresses in crust and mantle and the hemispherical magma ocean formed at impact, is dragged down to the core, resulting in an aspherical cone shape. (b) The positively buoyant silicate melt and crust are then dragged back up again. (c) A small melt pocket remains behind, below the newly formed patch of thickened crust.
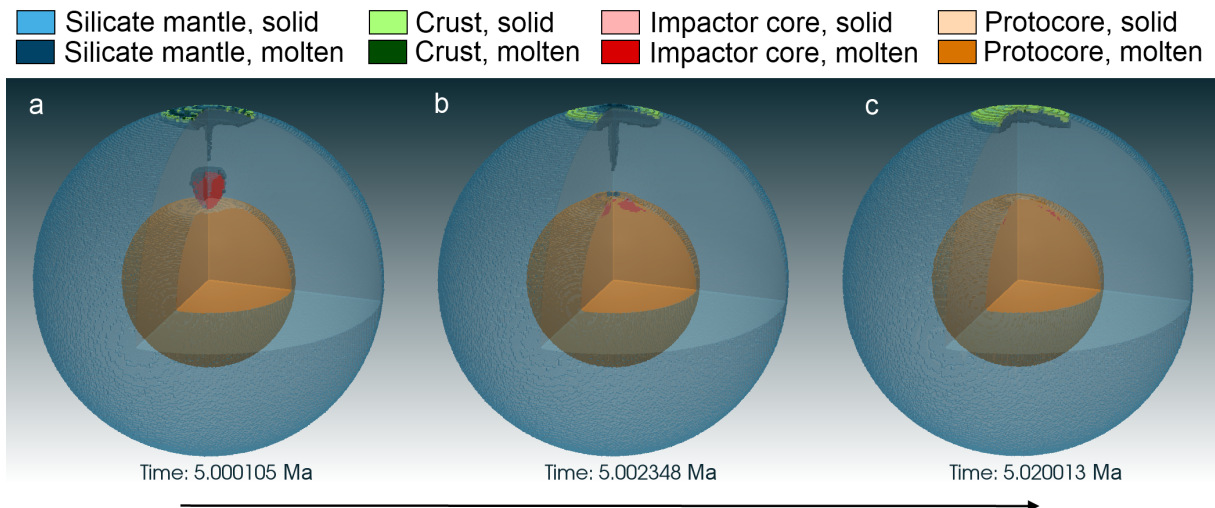
Figure 36: Crust and core formation for model *mars3Dd1* with a smaller impactor core. (a) due to the smaller impactor core, less silicate melt is produced at the impact site. The impactor also gets deformed on its down to the protocore. (b) Due to the temperature setup of the model, the impactor cannot penetrate the protocore (compare model *mars3Db1*). (c) Less crust is formed and the impactor seems to have almost no effect on the core at all.

Model	f_{diap}	$T_i\,[K]$	$T_p\,[K]$	$T_d\,[K]$	$r_{ic}\,[km]$	$\eta_{Si\ cut\ off}\,[Pa\,s]$	comment:
mars2D0o	1	1300	−	1300	500	10^{17}	initial model (old code)
mars2D0	1	1300	−	1300	500	10^{17}	initial model
mars2D1o	1	1800	−	1800	500	10^{17}	different Fe-Si temperature (old code)
mars2D1	1	1800	−	1800	500	10^{17}	different Fe-Si temperature
mars2D2	1	1700	−	1700	500	10^{17}	different Fe-Si temperature
mars2D3	1	1900	−	1900	500	10^{17}	different Fe-Si temperature
mars2D4	1	1800	−	1700	500	10^{17}	higher impactor core temperature
mars2D5	1	1900	−	1700	500	10^{17}	higher impactor core temperature
mars2D6	1	1900	−	1800	500	10^{17}	higher impactor core temperature
mars2D7	1	1700	−	1800	500	10^{17}	higher iron diapir temperature
mars2D8	1	1700	−	1900	500	10^{17}	higher iron diapir temperature
mars2D9	1	1800	−	1900	500	10^{17}	higher iron diapir temperature
mars2D10	1	2300	−	2300	500	10^{17}	very high iron temperature
mars2D11	1	2300	−	1700	500	10^{17}	very high impactor core temperature
mars2D12	1	2300	−	1900	500	10^{17}	very high impactor core temperature
mars2D13	1	1700	−	2300	500	10^{17}	very high iron diapir temperature
mars2D14	1	1900	−	2300	500	10^{17}	very high iron diapir temperature
mars3Da0	1	1300	−	1300	464	10^{17}	reference model: Fe-diapirs
mars3Da1	0	1300	1300	−	464	10^{17}	reference model: protocore
mars3Da2	0.5	1300	1300	1300	464	10^{17}	reference model: protocre with diapirs
mars3Db1	0	1300	1800	−	464	10^{17}	hot protocore
mars3Db2	0	1800	1300	−	464	10^{17}	hot impactor
mars3Db3	0	1800	1800	−	464	10^{17}	hot impactor and hot protocore
mars3Db4	0	1300	2500	−	464	10^{17}	very hot protocore
mars3Dc1	0	1800	1300	−	464	10^{19}	like b2, but higher cut-off viscosity in all silicates
mars3Dd1	0	1300	1800	−	232	10^{17}	like b1, but smaller impactor

Table 3: List of models

Model	$\bar{\rho}_{Si}\,[\frac{kg}{m^3}]$	$\bar{\rho}_{Fe}\,[\frac{kg}{m^3}]$	$\bar{\rho}_{bulk}\,[\frac{kg}{m^3}]$	$t\,[a]$
mars3Da0	3922.9	6574.0	4194.4	5.6618e+006
mars3Da1	3669.0	8612.1	4225.5	5.8983e+006
mars3Da2	3805.3	7272.1	4189.8	8.0342e+006
mars3Db1	3649.5	7521.5	4070.1	6.5680e+006
mars3Db2	3673.1	8587.1	4236.2	5.4774e+006
mars3Db3	3648.6	7533.9	4096.7	6.0948e+006
mars3Db4	3654.3	7483.5	4090.9	5.2353e+006
mars3Dc1	3669.1	8366.3	4193.3	5.8419e+006
mars3Dd1	3662.9	7534.9	4100.6	5.2725e+006

Table 4: $\bar{\rho}_{Si}$ denotes the mean density of silicate material, $\bar{\rho}_{Fe}$ denotes the mean density of iron material and $\bar{\rho}_{tot}$ denotes mean total density. All three density are taken at time t for each model.

Model	$\bar{T}_m\,[K]$	$\bar{T}_c\,[K]$	$\bar{T}_{tot}\,[K]$	$t\,[a]$
mars2D0		2111		
mars2D1		2415		
mars2D2		2351		
mars2D3		2481		
mars2D4		2359		
mars2D5		2368		
mars2D6		2422		
mars2D7		2405		
mars2D8		2465		
mars2D9		2472		
mars2D10		2725		
mars2D11		2404		
mars2D12		2515		
mars2D13		2676		
mars2D14		2693		
mars3Da0	1483.8	1640.9	1517.1	5.6618e+006
mars3Da1	1265.5	1412.4	1307.0	5.8983e+006
mars3Da2	1431.9	1604.7	1480.2	8.0342e+006
mars3Db1	1271.8	1815.3	1366.7	6.5680e+006
mars3Db2	1261.9	1419.0	1308.1	5.4774e+006
mars3Db3	1272.0	1824.7	1374.1	6.0948e+006
mars3Db4	1289.3	2399.9	1488.4	5.2353e+006
mars3Dc1	1282.9	1469.6	1339.2	5.8419e+006
mars3Dd1	1249.9	1773.3	1344.3	5.2725e+006

Table 5: $\bar{T}_m$ denotes the final mean temperature of the mantle, $\bar{T}_c$ is the mean temperature of the core and $\bar{T}_{tot}$ is total mean over the whole planet. All three temperatures are taken at time t for each model.

Model	$f_{Fe,vol}$	$f_{Fe,mass}$	$r_{core}\,[\%]$	time $[a]$
mars3Da0	0.102	0.161	0.468	5.6618e+006
mars3Da1	0.113	0.229	0.483	5.8983e+006
mars3Da2	0.111	0.193	0.480	8.0342e+006
mars3Db1	0.109	0.201	0.477	6.5680e+006
mars3Db2	0.115	0.232	0.486	5.4774e+006
mars3Db3	0.115	0.212	0.487	6.0948e+006
mars3Db4	0.114	0.209	0.485	5.2353e+006
mars3Dc1	0.111	0.223	0.481	5.8419e+006
mars3Dd1	0.113	0.208	0.484	5.2725e+006

Table 6: $f_{Fe,vol}$ denotes iron volume fraction and $f_{Fe,mass}$ denotes iron mass fraction. r_{core} is the final core radius relative to the the planets radius.